

Modeling of an Active Boring Bar

Tatiana Smirnova, Henrik Åkesson and Lars Håkansson

December 2007

Abstract

Vibration problems occurring during internal turning operations in the manufacturing industry urge for adequate passive and/or active control techniques in order to increase the productivity of machine tools. Usually, passive solutions are based on either boring bars made partly in high Young's modulus non-ductile materials such as sintered tungsten carbide or boring bars with tuned vibration absorbers adjusted to increase the dynamic stiffness in the frequency range of a certain resonance frequency of the boring bar. By utilizing an active boring bar with an embedded piezoceramic actuator and a suitable controller, the primary boring bar vibrations originating from the material deformation process may be suppressed with actuator-induced secondary "anti-" vibrations. In order to design an active boring bar, several issues have to be addressed, i.e., selecting the characteristics of the actuator, the actuator size, the position of the actuator in the boring bar, etc. This usually implies the manufacturing and testing of several prototypes of an active boring bar, and this is a time-consuming and costly procedure. Therefore, mathematical models of active boring bars incorporating the piezo-electric effect that enable the accurate prediction of their dynamic properties and responses are of great importance. This report addresses the development of a "3-D" finite element model of the system "boring bar-actuator-clamping house". The spatial dynamic properties of the active boring bar, i.e., its natural frequencies and mode shapes, as well as the transfer function between actuator voltage and boring bar acceleration are calculated based on the "3-D" FE model and compared to the corresponding experimentally obtained estimates. Two types of approximations of the Coulomb friction force, the arctangent and the bilinear models, are evaluated concerning modeling contact between the surface of the boring bar and the clamping house.

Contents

1	Introduction	5
2	Materials and Methods	10
2.1	Experimental Setup	10
2.1.1	System Overview	10
2.1.2	Measurement Equipment and Setup	14
2.1.3	System Identification	16
2.2	Experimental Modal Analysis	19
2.3	Euler-Bernoulli Model of an Active Boring Bar	20
2.4	"3-D" Finite Element Model	25
2.4.1	Model of the system "boring bar - clamping house"	25
2.4.2	Model of the Actuator	26
2.4.3	Contact Modeling in the Finite Element Analysis	28
2.4.4	Coulomb Friction Modeling	32
2.4.5	Transient response	35
2.4.6	Harmonic response	36
2.5	SDOF Nonlinear Model	37
3	Results	38
3.1	Modal Analysis Results	39
3.1.1	Natural Frequencies	39
3.1.2	Mode Shapes	39
3.2	System Identification	41
3.2.1	Experimentally Estimated Accelerance	41
3.2.2	Harmonic Response Based on FEM	41
3.2.3	Transient Response Based on FEM	43
3.3	Dynamic Modeling of the Boring Bar with the Coulomb Friction Force Included	45
3.3.1	Transient Response Based on the SDOF Model	45

3.3.2	Dynamics of the "3-D" Finite Element Model Enabling Variable Contact between the Boring Bar and the Clamping House and also with Coulomb Friction Force	49
3.4	Actuator Receptance	52
4	Summary and Conclusions	56

Chapter 1

Introduction

The internal turning operation is generally considered as one of the most vibration-prone metal working processes. In such operations, a boring bar is used to machine deep, precise geometries to required tolerances inside a pre-drilled hole in a workpiece. A boring bar can usually be characterized as a slender beam and is generally the weakest link in a machine tool system. During turning, the material deformation process induces a broad-band excitation of the machine tool, and, as a result, relative dynamic motion between the boring bar and the workpiece frequently occurs, commonly referred to as chatter. High levels of boring bar vibration result in poor surface finish, excessive tool wear, tool breakage and severe levels of acoustic noise. Thus, boring bar vibration has a negative impact on productivity, working environment, etc. Usually, the high vibration level is excited at the natural frequencies related to low-order bending modes of the boring bar and are dominated by the bending mode in the cutting speed direction, since it is in this direction that the cutting force has the largest component [1, 2, 3]. In industry, there are considerable demands concerning methods improving the stability of internal turning operations. The motive is mainly to increase the productivity, but the working environment is also a growing issue.

From at least the beginning of the twentieth century, research in metal cutting has been devoted to expanding the existing knowledge of cutting dynamics, etc., by means of mathematical modeling and experimental studies [4, 5, 6, 3, 7, 8, 9]. Most research carried out on the dynamic modeling of cutting dynamics has concerned the prediction of stability limits, i.e., predicting cutting data for stable cutting [3, 8].

The strategies for controlling boring bar vibrations can be classified into two directions. The first direction refers to control of cutting data in order to maintain stable cutting, i.e., to avoid cutting data resulting in chatter or to continuously vary cutting data in a structured manner to avoid chatter

[9, 10, 11]. The second direction concerns modifications of the dynamic stiffness of one or several parts of the chain insert - tool holder - clamping - machine tool, with the purpose of increasing the system's resistance to machine tool chatter [9, 12, 13, 14, 15, 16]. Generally, the boring bar vibration control methods modifying the dynamic stiffness are divided into two groups: passive and active control. In passive boring bar vibration control, the dynamic stiffness may be increased by changing the static stiffness of the bar, e.g., for instance by using a boring bar produced completely or partly (composite boring bar) of materials with higher modulus of elasticity such as sintered tungsten carbide [9, 12]. Another passive control strategy is to use passive Tuned Vibration Absorbers (TVA) to resist machine tool chatter [9, 12]. A TVA consists of a tube which contains a reactive mass inside a layer of damper oil and is usually built into the boring bar close to the tool tip [12, 13]. TVA boring bars offer solutions with a fixed enhancement of the dynamic stiffness, frequently tuned for a narrow frequency range comprising the fundamental bending modes eigenfrequencies [9]. On the other hand, active feedback control of turning operations produces a selective increase of the dynamic stiffness at the actual frequency of the dominating bending mode [14, 15, 16].

An active control approach was reported by Tewani et al. [14] concerning active dynamic absorbers in boring bars controlled by a digital state feedback controller. It was claimed to provide a substantial improvement in the stability of the cutting process. Browning et al. [15] reported an active clamp for boring bars controlled by a feedback version of the filtered-x LMS algorithm. They assert that the method enables one to extend the operable length of boring bars. Claesson and Håkansson [16] controlled tool vibration by using the feedback filtered-x LMS algorithm to control tool shank vibration in the cutting speed direction, without applying the traditional regenerative chatter theory.

Two important constraints concerning the active control of tool vibration involve the difficult environment in a lathe and industry demands. It is necessary to protect the actuator and sensors from the metal chips and cutting fluid. Also, the active control system should be applicable to a general lathe. Pettersson et al. [17] reported an adaptive active feedback control system based on a tool holder shank with embedded actuators and vibration sensors. This control strategy was later applied to boring bars by Pettersson et al. [18]. Åkesson et al. [19] reported the successful application of the active adaptive control of boring bar vibration in industry using an active boring bar with embedded actuators and vibration sensors.

The active control of boring bar vibration is based on an active boring bar equipped with embedded actuators and vibration sensors in conjunction with a feedback controller. The active boring bar typically has an accelerometer

attached close to the tool-end, which measures boring bar vibration in the cutting speed direction. The controller uses the accelerometer signal to produce secondary or "anti-" vibrations via an actuator embedded inside a groove milled in the longitudinal direction below the center line of the boring bar. Due to the piezoelectrical properties of the actuator material, the dynamic control signal will steer the length expansion of the actuator. The actuator will in turn apply a bending moment to the boring bar to counteract the primary vibration excited by the material deformation process [20].

In order to design an active boring bar with embedded actuator, several issues have to be addressed, i.e., selecting the characteristics of the actuator, the actuator size, the position of the actuator in the boring bar, etc. Obtaining adequate performance from an active boring bar usually implies the manufacturing and testing of several prototypes of the active boring bar, this is a complex, time consuming and costly procedure. Thus, it is likely that the efficiency of design procedure can be increased by means of dynamic modeling of active boring bar, for instance, by utilizing "3-D" finite element modeling. It is plausible that such a model can be used, e.g., for predicting of the dynamic properties of an active boring bar, describing the interaction of the boring bar and actuator, and accounting for nonlinearities introduced into its response by the contact between the boring bar, clamping house and clamping screws.

A number of research works have been carried out concerning the modeling of a boring bar as a system with a large but finite number of degrees-of-freedom, using finite element analysis. Wong [21] used Timoshenko beam finite elements to model a boring bar. He designed an electromagnetic dynamic absorber and simulated its performance, utilizing modal control and direct feedback control based on the finite element model of the boring bar. Wong claims that both controllers succeed in significant damping of boring bar vibrations at the lowest vibration mode. Nagano [22] used pitched-based carbon fiber reinforced plastic (CFRP) material to develop a chatter resistant boring bar with a large overhang. He made an attempt to create a "3-D" finite element model in order to predict natural frequencies and improve dynamic characteristics of the boring bar by modeling embedded steel cores of various shapes. The cutting performance and stability of the designed boring bars regarding chatter were investigated experimentally. He claims that utilization of the CFRP material together with the cross-shaped steel core allows for the successful stable machining for boring bars with length-to-diameter of more than seven. Nagano also mentioned the necessity concerning the development of improved models for the clamping of the boring bar. Later, Sturesson et al. [23] developed a "3-D" finite element model of a tool holder shank. They used normal mode analysis to evaluate the natural frequencies, modal masses and mode participation factors of the tool holder shank. The modal damping

was estimated using the free vibration decay method. The spectral densities' estimates were also utilized to obtain natural frequencies. The results of the normal mode analysis and spectral densities' estimates were well-correlated. Baker et al. [24] used FEM in the stability analysis of a turning operation. He approximated the cutting force by using the orthogonal cutting force model. Baker also based his method of stability prediction on the assumption of the linearity of the tooling structure's behavior. Two different types of FE models were considered: firstly, "1-D" FE models of the tool holder and the workpiece attached to the rigid base; secondly, "3-D" FE models of the tool holder and the workpiece attached to the deformable "3-D" FE model of machine tool. The FE models were used to extract structural matrices, with the purpose of using them in stability analysis. The maximum stable width of cut was predicted for a set of geometric dimensions of the tool holder and the workpiece (for both types of models) as a function of spindle speed. However, no experimental results were presented. Later, in [25], Mahdavinejad also tried to predict maximum width of cut, ensuring stable cutting with the use of a "3-D" FE model of a machine tool. Several "3-D" FE models containing different machine tool parts were developed. Natural frequencies and the mode shapes of the tailstock were estimated based on the "3-D" FE models and compared with results obtained from experimental modal analysis. The stability lobe diagrams were obtained for the chuck-center with and without tailstock cases. In both cases the stability lobe diagrams were calculated based on analytical considerations and experiments. Results from the modal analysis as well as the stability lobe diagrams produced with the use of FE models are claimed to be well-correlated to corresponding experimental estimates.

Thus, it appears as though no work has been carried out on the finite element modeling of active boring bars with embedded piezoelectric stack actuators.

This report addresses the process of developing a "3-D" finite element model of the system "boring bar - actuator - clamping house". Estimates of the first two natural frequencies and the corresponding mode shapes have been produced based on both an initial linear "3-D" finite element model and an experimental modal analysis of the active boring bar, and also compared. A more advanced nonlinear "3-D" finite element model of the active boring bar, enabling variable contact between clamping house and boring bar, has also been considered. As a further extension of this "3-D" finite element model, a model that incorporates nonlinear friction force acting between the contacting surfaces of the boring bar and clamping house has been evaluated. Two different models of the Coulomb friction force, the bilinear and the arctangent, have been considered. The nonlinear active boring bar FE models were evaluated in comparison with the experimental modal analysis results. Estimates

of control path frequency response functions between the voltage applied to the actuator and the acceleration in the position of the error accelerometer in the cutting speed direction and in the cutting depth direction, have been produced. These frequency response functions were estimated both for data obtained from the numerical simulations using the "3-D" finite element models and for experimental data from the lathe. Also, a simple distributed-parameter Euler-Bernoulli model of the active boring bar has been introduced.

Chapter 2

Materials and Methods

2.1 Experimental Setup

2.1.1 System Overview

The experimental modal analysis and control path estimates were conducted in a Mazak SUPER QUICK TURN - 250M CNC turning center. The machine tool has a spindle power of 18.5 kW and a maximal machining diameter of 300 mm, a maximal spindle speed of 4000 (r.p.m.), with 1007 mm between the centers and a turret capacity of 12 tools (see Fig. 2.1).



Figure 2.1: Mazak 250 SUPER QUICK TURN - 250M CNC turning center.

Active Boring Bar

The active boring bar was based on a standard boring bar, S40T PDUNR15 F3 WIDAX (see Fig. 2.2). The WIDAX boring bar is made of the material 30CrNiMo8; in the modeling, it is assumed that Young's elastic modulus $E = 205 \text{ GPa}$, density $\rho = 7850 \text{ kg/m}^3$ and Poisson's coefficient $\nu = 0.3$.

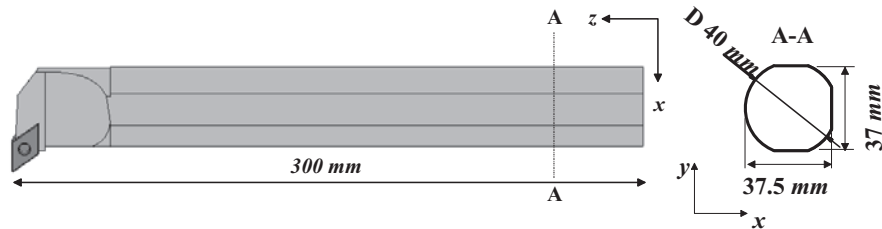


Figure 2.2: Top-view and cross-section of a standard boring bar, S40T PDUNR15 F3 WIDAX.

It has an actuator embedded into a milled space below the center line of the boring bar and an accelerometer attached close to the insert (see Fig. 2.3).

The coordinate system is defined as follows: x is the cutting depth direction, y is the negative cutting speed direction and z is the feed direction.

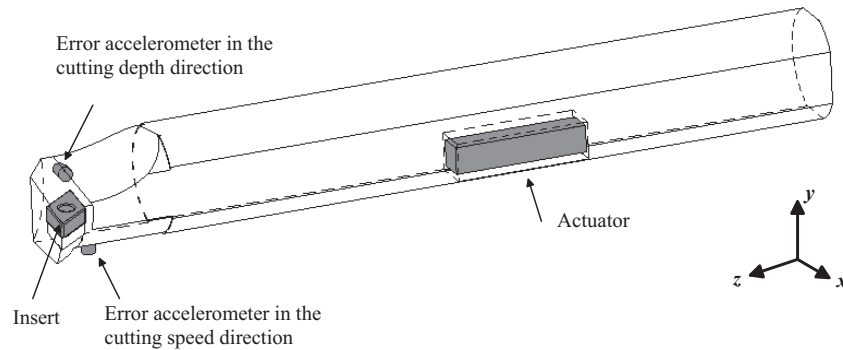


Figure 2.3: Schematic view of an active boring bar.

Clamping House

As a clamping house, a standard 8437-0 40 mm Mazak holder was used (see Fig. 2.4). The clamping house is attached to the turret by four screws. The boring bar can be clamped in the clamping house using either four or six

screws. In the experiments and simulations presented in the current report, only four screws were used to clamp the boring bar.

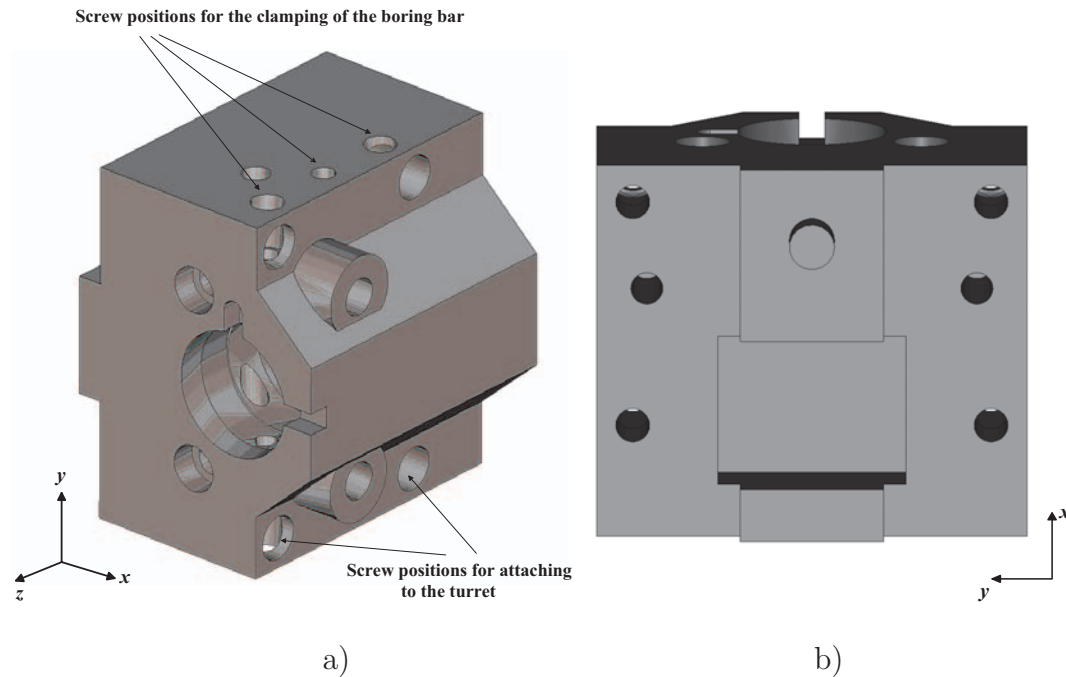


Figure 2.4: Standard 8437-0 40 mm Mazak holder: a) general view; b) view of the side for the turret contact.

Piezoelectric Actuator

The piezoelectric stack actuator used in the experiments is made of the piezoelectric material Lead Zirconate Titanate (PZT-5H) and is shown in Fig. 2.5. The actuator material properties (in the finite element modeling) were chosen as they are similar to the properties of PZT-5H material, with modifications made for the strain coefficients d_{33} and d_{31} in order to match the specification for the maximum stroke of the actuator [26, 27]. The actuator specifications are given in Table 2.1, [26, 27].

Furthermore, the piezoelectric material properties such as the elastic coefficient matrix $[\mathbf{c}^E]$, the dielectric matrix $[\boldsymbol{\varepsilon}]$ and the piezoelectric matrix $[\mathbf{e}]$ for this material are given in Eq. 1, Eq. 2 and Eq. 3 respectively [26, 27].

Property name	Value
Actuator material	PZT-5H
Free expansion ΔL_a , [m]	38×10^{-6}
Strain coefficient d_{33} , [m/V]	640×10^{-12}
Max operating voltage (P-P) V_{max} , [V]	150
Density ρ , [kg/m^3]	7500
Actuator stiffness k_a , [N/m]	125×10^6

Table 2.1: Actuator specifications.

$$[\mathbf{c}^E] = \begin{bmatrix} 12.72 & 8.02 & 8.47 & 0 & 0 & 0 \\ 8.02 & 12.72 & 8.47 & 0 & 0 & 0 \\ 8.47 & 8.47 & 11.74 & 0 & 0 & 0 \\ 0 & 0 & 0 & 2.30 & 0 & 0 \\ 0 & 0 & 0 & 0 & 2.30 & 0 \\ 0 & 0 & 0 & 0 & 0 & 2.35 \end{bmatrix} \times 10^{10}, [Pa] \quad (2.1)$$

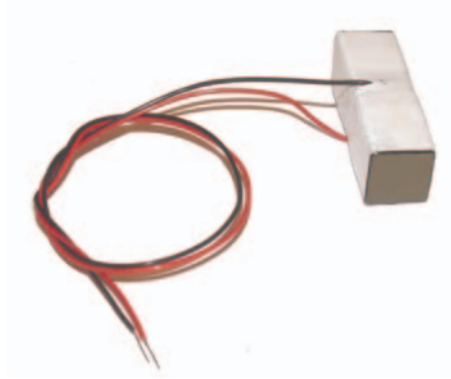


Figure 2.5: Piezoelectric stack actuator.

$$[\mathbf{e}] = \begin{bmatrix} 0 & 0 & -6.62 \\ 0 & 0 & -6.62 \\ 0 & 0 & 23.24 \\ 0 & 17.03 & 0 \\ 17.03 & 0 & 0 \\ 0 & 0 & 0 \end{bmatrix}, [C/m^2] \quad (2.2)$$

$$[\varepsilon] = \begin{bmatrix} 27.71 & 0 & 0 \\ 0 & 27.71 & 0 \\ 0 & 0 & 30.10 \end{bmatrix} \times 10^{-9}, [F/m] \quad (2.3)$$

2.1.2 Measurement Equipment and Setup

The following equipment was used to carry out experimental modal analysis:

- 12 PCB 333A32 accelerometers;
- 1 Ling Dynamic Systems shaker v201;
- 1 Gearing & Watson Electronics shaker v4
- 2 Brüel & Kjær 8001 impedance heads;
- HP VXI E1432 front-end data acquisition unit;
- PC with IDEAS Master Series version 6.

The boring bar was simultaneously excited in the cutting speed direction and cutting depth direction by two shakers via impedance heads attached at the distance $l_1 = 100$ mm from the clamped end of the active boring bar (see Figure 2.6). The spatial motion of the boring bar was measured by 12 accelerometers and 2 impedance heads glued with the distance of $l_2 = 25$ mm from each other starting at 25 mm from the free end of the boring bar: 6 accelerometers and one impedance head in the cutting speed direction and 6 accelerometers and the other impedance head in the cutting depth direction.

The following equipment was used to carry out control path identification:

- 2 PCB 333A32 accelerometers;
- 1 KEMO Dual Variable Filter VBF 10M;
- A custom designed amplifier for capacitive loads;
- HP VXI E1432 front-end data acquisition unit;
- PC with IDEAS Master Series version 6.

During the control path identification, the active boring bar, clamped in the lathe, was excited by means of voltage applied over the actuator. The response of the boring bar was measured by two accelerometers located at the error sensor positions, which were at a distance of 25 mm from the free end of the boring bar in the cutting speed and cutting depth direction respectively.

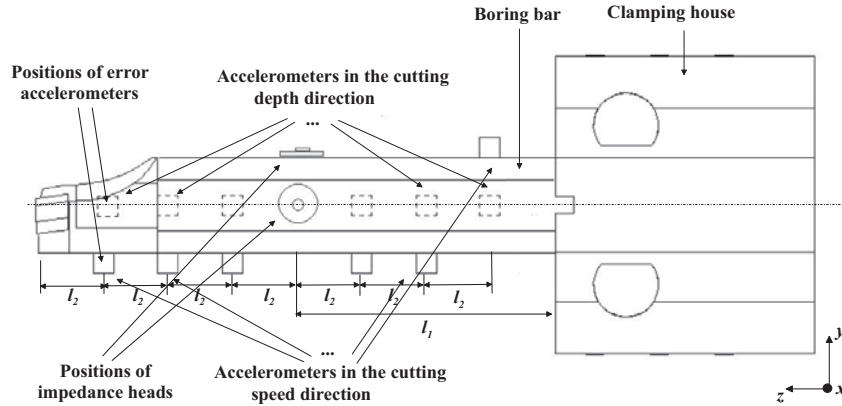


Figure 2.6: Drawing of the clamped active boring bar with accelerometers and cement studs for the attachment of impedance heads.

Also system identification was carried out for the transfer paths between the voltage applied to the actuator and the strain measured at the points P1, P2, P3 and P4 close to the "boring bar - actuator" interfaces (see Fig. 2.7). Four KYOWA strain gages were used for this purpose.

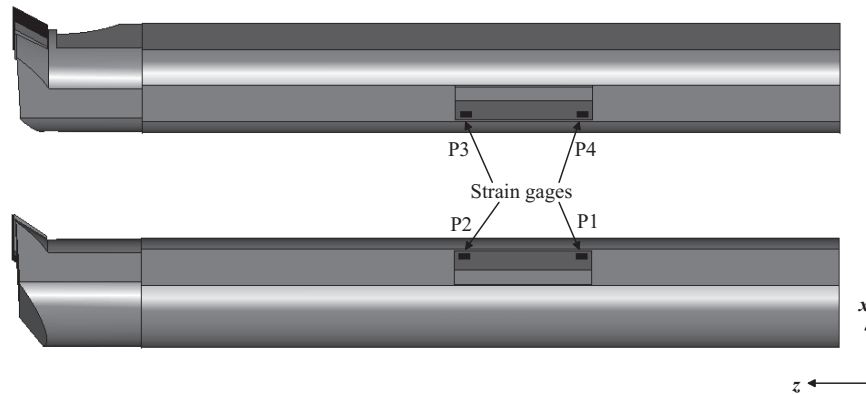


Figure 2.7: Drawing of the active boring bar with strain gages positions.

2.1.3 System Identification

System identification in general concerns the production of a mathematical model of the dynamic properties of an unknown system, based on experimentally obtained data. In the case of mechanical systems, system identification usually implies estimating the frequency response functions between an input excitation force signal and an output signal which can be displacement, velocity or acceleration. Since it is most convenient to measure the acceleration of a mechanical system, acceleration frequency response functions are frequently considered.

Spectral properties The frequency response function can be estimated as a ratio of the cross-power spectral density between the excitation and the response signals and the power spectral density of the excitation signal. Most of the non-parametric methods for spectrum estimation are based on the averaging of periodograms [28]. The most general is Welch's method, which allows one to average modified periodograms, which are produced based on the windowed sequences of a signal that may be overlapping to a certain extent.

The double-sided power spectral density of a discrete time signal $x(n)$ can be estimated using Welch's method as follows [28]:

$$\hat{P}_{xx}^{PSD}(f_k) = \frac{1}{MF_s \sum_{n=0}^{N-1} w^2(n)} \sum_{m=0}^{M-1} \left| \sum_{n=0}^{N-1} x_m(n)w(n)e^{-j2\pi nk/N} \right|^2 \quad (2.4)$$

$$f_k = \frac{k}{N}F_s$$

where N is the block length or periodogram length, $k = 0, \dots, N-1$, $x_m(n) = x(n+mD)$, $m = 0, 1, \dots, M-1$ is the data segment of the signal $x(n)$ with the length L , M is the number of periodograms, D is the overlapping increment, i.e., for 50% overlap $D=N/2$, F_s is the sampling frequency and $w(n)$ is the window function. In the case of power spectral density estimation, the Hanning window is commonly used [28].

In practice, the excitation and response signals can be corrupted with noise. Depending on whether the noise is affecting the measured excitation signal or response signal, frequency response function estimators appropriate for the respective case may be utilized. The H_1 estimator is usually implemented in FFT-analyzers [29] and may be used when noise is only assumed to corrupt the response signal.

$$\hat{H}_1(f_k) = \frac{\hat{P}_{yx}^{PSD}(f_k)}{\hat{P}_{xx}^{PSD}(f_k)} \quad (2.5)$$

The \hat{H}_2 estimator is used when noise is assumed to only affect the measured excitation signal.

$$\hat{H}_2(f_k) = \frac{\hat{P}_{yy}^{PSD}(f_k)}{\hat{P}_{yx}^{PSD}(f_k)} \quad (2.6)$$

The quality of the frequency response function estimate can be evaluated via the coherence function estimate $\hat{\gamma}_{yx}^2$, which is the ratio of two estimators [30].

$$\hat{\gamma}_{yx}^2(f_k) = \frac{\hat{H}_1(f_k)}{\hat{H}_2(f_k)} = \frac{|\hat{P}_{yx}^{PSD}(f_k)|^2}{\hat{P}_{xx}^{PSD}(f_k)\hat{P}_{yy}^{PSD}(f_k)} \quad (2.7)$$

The normalized random error of the frequency response function's magnitude function estimate can be estimated according to [30]:

$$\varepsilon_r[|\hat{H}_{xy}(f_k)|] \approx \frac{(1 - \hat{\gamma}_{xy}^2(f_k))^{1/2}}{\sqrt{2\hat{\gamma}_{xy}^2(f_k)M_e}} \quad (2.8)$$

where M_e is the equivalent number of averages. The equivalent number of averages is given by [31]:

$$M_e = \frac{M}{1 + 2 \sum_{m=1}^{M-1} \frac{M-m}{M} \varrho(m)} \quad (2.9)$$

where $\varrho(m)$ is given by [31]:

$$\varrho(m) = \frac{\left[\sum_{n=0}^{N-1} w(n)w(n+mD) \right]^2}{\left[\sum_{n=0}^{N-1} w^2(n) \right]^2} \quad (2.10)$$

In the case when power and cross-power spectral densities estimates are produced without the overlapping of data blocks, $M_e = L/N$. This typically corresponds to the case when burst random noise is used as an excitation signal.

The normalized random error for the coherence function can be estimated by [30]:

$$\varepsilon_r[\hat{\gamma}_{xy}^2(f)] \approx \frac{\sqrt{2}(1 - \hat{\gamma}_{xy}^2(f))}{\sqrt{\hat{\gamma}_{xy}^2(f)M_e}} \quad (2.11)$$

The normalized random error of the multiple coherence function is given by [30]:

$$\varepsilon_r[\hat{\gamma}_{y:x}^2(f)] \approx \frac{\sqrt{2}[1 - \hat{\gamma}_{y:x}^2(f)]}{\sqrt{\hat{\gamma}_{y:x}^2(f)(M_e + 1 - s)}} \quad (2.12)$$

where s is the number of excitation signals.

The power spectral density estimation parameters used in the production of the experimental control path frequency response function estimates are summarized in Table 2.2.

Parameter	Value
Signal type	True random
Excitation frequency range	0-1000 Hz
Sampling frequency, F_s	2560
Number of spectral lines, N	3201
Frequency resolution, Δf	0.3125 Hz
Number of averages	200
Window	Hanning
Overlap	50 %

Table 2.2: Parameters for the experimental spectral density estimation.

The power spectral density estimation parameters used in the production of the numerical control path frequency response function estimates are summarized in Table 2.3.

Parameter	Value
Signal type	True random
Excitation frequency range	0-1000 Hz
Sampling frequency, F_s	1536 Hz
Number of spectral lines, N	1536
Frequency resolution, Δf	1 Hz
Number of averages	5
Window	Hanning
Overlap	50 %

Table 2.3: Parameters for the spectral density estimation concerning the finite element models.

2.2 Experimental Modal Analysis

In the concept of experimental modal analysis, the boring bar is considered as a multiple degree-of-freedom system. Excitation forces and responses are measured spatially at discrete positions on the boring bar and collected simultaneously for subsequent parameter estimation or curve fitting. Experimental modal analysis allows for the identification of a system's modal parameters: natural frequencies, mode shapes and relative damping ratios. Experimental modal analysis serves as a tool for, e.g., the verification and updating of finite element models [?]. The theory and methods of experimental modal analysis are essentially built on four assumptions: the system is linear, the system is time-invariant, the system is observable and the system obeys Maxwell's reciprocity theorem [32].

Parameter Estimation In the concept of the experimental modal analysis the boring bar is modeled as a system with N_{ema} degrees-of-freedom. The boring bar vibration can be described by the equation of motion in matrix form.

$$[\mathbf{M}]\{\ddot{\mathbf{w}}(t)\} + [\mathbf{C}]\{\dot{\mathbf{w}}(t)\} + [\mathbf{K}]\{\mathbf{w}(t)\} = \{\mathbf{f}(t)\} \quad (2.13)$$

where N_{ema} is the number-of-degrees of freedom, the matrix $[\mathbf{M}]$ is the $N_{ema} \times N_{ema}$ mass matrix, $[\mathbf{C}]$ is the $N_{ema} \times N_{ema}$ damping matrix and $[\mathbf{K}]$ is the $N_{ema} \times N_{ema}$ elastic stiffness matrix. Vector $\{\mathbf{f}(t)\}$ is the space- and time-dependent load vector. Vector $\{\mathbf{w}(t)\}$ is the space- and time-dependent displacement vector. Its i -th element contains displacement measured in the point with coordinates (x_i, y_i, z_i) and $i = 1, \dots, N_{ema}$ at time instant t . The displacement vector may be written as:

$$\{\mathbf{w}(t)\} = \left\{ \begin{array}{c} w(x_1, y_1, z_1, t) \\ w(x_2, y_2, z_2, t) \\ \vdots \\ w(x_{N_{ema}}, y_{N_{ema}}, z_{N_{ema}}, t) \end{array} \right\} \quad (2.14)$$

The spatial dynamic properties of the boring bar were identified using the time-domain polyreference least squares complex exponential method [29]. This method is based on the discrete-time version of the impulse response function matrix:

$$[h(n)] = \sum_{r=1}^{N_{ema}} ([A]_r e^{\lambda_r T_s n} + [A^*]_r e^{-\lambda_r T_s n}) = \sum_{r=1}^{2N_{ema}} [A]_r e^{\lambda_r T_s n} \quad (2.15)$$

where $[A]_r = Q_r \{\psi\}_r \{\psi\}_r^T$ and $\lambda_r = 2\pi(-f_r \zeta_r + j f_r \sqrt{1 - \zeta_r^2})$, $\{\psi\}_r$ is the $N_{ema} \times 1$ mode shape vector, ζ_r is the modal damping ratio, f_r is the undamped system's eigenfrequency, Q_r is the modal scaling factor and T_s is the sampling time interval. An estimate of the impulse response function matrix $[\hat{h}(n)]$ is produced based on the Inverse Fourier Transform of an estimate of the receptance matrix $[\hat{H}_r(f_k)]$. The estimate of the receptance matrix $[\hat{H}_r(f_k)]$ is assembled based on power spectral density estimates of the measured excitation forces and the cross-power spectral density estimates between the measured output responses and excitation forces.

Based on the simultaneously estimated impulse responses, between each of the input forces locations and all of the output response locations, the polyreference least squares complex exponential method utilizes Prony's method and the least squares method in the production of global estimates of eigenfrequencies f_r , damping ratios ζ_r and mode shapes $\{\psi\}_r$ [32, 29].

The orthogonality of extracted mode shapes $\{\psi_{EMA}\}_i$ and $\{\psi_{EMA}\}_j$, $i, j \in \{1, 2, \dots, N_{ema}\}$, may be evaluated using the Modal Assurance Criterion [32]:

$$MAC_{ij} = \frac{|\{\psi_{EMA}\}_i^T \{\psi_{EMA}\}_j|^2}{(\{\psi_{EMA}\}_i^T \{\psi_{EMA}\}_i)(\{\psi_{EMA}\}_j^T \{\psi_{EMA}\}_j)} \quad (2.16)$$

The Modal Assurance Criterion may also be used to provide a measure on the correlation between the experimentally-measured mode shapes $\{\psi_{EMA}\}_i$ and the numerically-calculated mode shapes $\{\psi_{FEM}\}_j$ of, e.g., a finite element model.

$$MAC_{ij} = \frac{|\{\psi_{EMA}\}_i^T \{\psi_{FEM}\}_j|^2}{(\{\psi_{EMA}\}_i^T \{\psi_{EMA}\}_i)(\{\psi_{FEM}\}_j^T \{\psi_{FEM}\}_j)} \quad (2.17)$$

The parameters used in the modal analysis of the clamped active boring bar can be found in Table 2.4.

2.3 Euler-Bernoulli Model of an Active Boring Bar

A distributed-parameter Euler-Bernoulli beam model [33, 34] can be used to describe the dynamic motion of an active boring bar. The Euler-Bernoulli beam model considers only transverse beam vibrations and ignores shear deformation and rotary inertia [35, 36]. A "clamped-free" model of the active boring bar is shown in the Fig. 2.8. The sign convention used for displacement, forces and moment is as follows: forces and displacements in the positive directions of the coordinate systems axes are positive, and a moment about a

Parameter	Value
Signal type	Burst random (90/10)
Excitation frequency range	300-800 Hz
Sampling frequency, F_s	1280
Number of spectral lines, N	1601
Frequency resolution, Δf	0.3125 Hz
Number of averages	200
Window	Rectangular
Frequency range for curve fitting	400-600 Hz

Table 2.4: Modal analysis parameters.

coordinate system axis that is in the counterclockwise direction if viewed from the end of the coordinate system axis towards the origin is considered to be positive. If one assumes that the geometric features of the boring bar tool-end are negligible to overall boring bar dynamics, i.e., that cross-sectional area $A(z)$ and cross-sectional moment of inertia around x axis $I_x(z)$ are constants, then the Euler-Bernoulli partial differential equation of the boring bar transverse vibrations in the cutting speed direction may be written as [19, 35, 37, 38]:

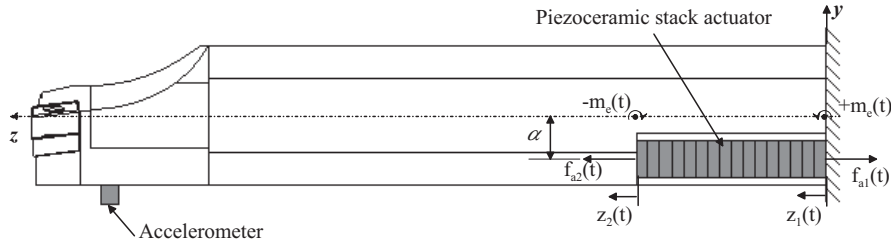


Figure 2.8: The "clamped-free" model of the active boring bar.

$$\rho A \frac{\partial^2 w(z, t)}{\partial t^2} + EI_x \frac{\partial^4 w(z, t)}{\partial z^4} = \frac{\partial m_e(z, t)}{\partial z} \quad (2.18)$$

where ρ is the density of the boring bar material, $w(z, t)$ is the deflection in y direction, E is the Young's elastic modulus and $m_e(z, t)$ is the space- and time-dependent external moment load per unit length.

The cross sectional area A , the moments of inertia around "x"-axis I_x and around "y"-axis I_y were calculated assuming that the distributed-parameter

model of the active boring bar has a constant cross-section as shown in Fig. 2.2. The calculated boring bar's cross-sectional properties are summarized in Table 2.5.

Property	Cutting speed direction	Cutting depth direction	Units
l	0.2		m
A	1.1933×10^{-3}		m^2
I	1.1386×10^{-7}	1.1379×10^{-7}	m^4

Table 2.5: Properties used in Euler-Bernoulli model calculations.

To obtain the forced response of the beam, the expansion theorem can be utilized [36], i.e., the time-domain dynamic response of the boring bar can be expressed as:

$$w(z, t) = \sum_{r=1}^{\infty} \psi_r(z) y_r(t) \quad (2.19)$$

where $\psi_r(z)$, $1 \leq r$ are the normal modes determined by the boundary conditions for the beam and the normalization of the eigenfunctions or mode shapes, and $y_r(t)$ is the modal displacement. Each modal displacement $y_r(t)$ can be determined as a forced response of an undamped mechanical system, which is usually referred to as Duhamel's integral [39].

$$y_r(t) = \frac{1}{m_r 2\pi f_r} \int_0^t f_{load,r}(\tau) \sin(2\pi f_r(t - \tau)) d\tau \quad (2.20)$$

where m_r is the modal mass, f_r is the undamped system's eigenfrequency, $f_{load,r}(t)$ is the generalized load for mode r . In the case of an external moment load, the generalized load for mode r , $f_{load,r}(t)$ is given by:

$$f_{load,r} = \int_0^l \psi_r(z) \frac{\partial m_e(z, t)}{\partial z} dz \quad (2.21)$$

where l is the length of the beam, i.e., the length of the boring bar overhang.

Due to the piezoelectric properties of actuator material, the actuator expands under the applied voltage. The expansion of the actuator is, however, constrained at the "boring bar - actuator" interfaces. As the actuator exhibits elastic behavior, some part of its free expansion will be lost and transformed into loads applied to the boring bar: $f_{a1}(t)$ and $f_{a2}(t)$, in parallel with the "z"-axis. This, in turn will cause displacements $z_1(t)$ and $z_2(t)$ of the boring bar in "boring bar - actuator" interfaces. Because of the position of the actuator, i.e., it is placed below the central line of the boring bar with the distance

α , the loads applied by the actuator result in the bending and stretching of the boring bar. The dynamics of the actuator - boring bar interaction can be described in terms of point receptances at the respective actuator interface of the active boring bar. Assuming that the Fourier Transform of the responses $Z_1(f)$ and $Z_2(f)$ and of the loads, $F_{a1}(f)$ and $F_{a2}(f)$ (where f is frequency) exists, the point receptances may be expressed as:

$$H_1(f) = -\frac{Z_1(f)}{F_{a1}(f)} \quad (2.22)$$

respective

$$H_2(f) = \frac{Z_2(f)}{F_{a2}(f)} \quad (2.23)$$

Assuming that the actuator operates below its resonance frequency, thus neglecting the inertial effects of the actuator, the force that the actuator exerts on the boring bar, $F_a(f) = -F_{a1}(f) = F_{a2}(f)$, may approximately be related to the constraint expansion or motion of the actuator, the relative displacement $Z(f) = Z_2(f) - Z_1(f)$, according to [37]:

$$F_a(f) = \frac{E_a A_a}{L_a} (\Delta L_a(f) - Z(f)) \quad (2.24)$$

where $F_a(f)$ is the Fourier Transform of the internal force that the actuator applies, A_a is the cross-sectional area of the actuator's piezoelectric material, E_a is the Young's elastic modulus of the actuator's piezoelectric material and $\Delta L_a(f)$ is the Fourier Transform of the free expansion of an unloaded piezoelectric stack actuator (see Eq. 2.32). If the point receptances at the respective actuator end are summed to form the receptance $H_B = H_1(f) + H_2(f)$, the relative displacement $Z(f)$ may be expressed as:

$$Z(f) = H_B(f) F_a(f) \quad (2.25)$$

Using a force balance combining Eq. 2.24, Eq. 2.25 and the Fourier Transform of the expression for the free expansion of an unloaded piezoelectric stack actuator in Eq. 2.32 yields an expression for the actuator force applied on the boring bar as a function of actuator voltage $V(f)$ [37]:

$$F_a(f) = \frac{k_a \eta d_{33}}{1 + k_a H_B(f)} V(f) = H_{fv}(f) V(f) \quad (2.26)$$

where k_a is the actuator equivalent spring constant, η is the number of piezoelectric layers in the actuator, d_{33} is the piezoelectric strain constant, $H_{fv}(f)$ is the electro-mechanic frequency response function between the input voltage $V(f)$ and the output actuator force $F_a(f)$.

Assume that the natural surface of the boring bar (in the section where actuator is situated) coincides with the "z"-axis, and that the "y"-axis is normal to the natural surface. The distance, then, between the "boring bar - actuator" interface and the natural surface of the boring bar is α , as shown in Fig. 2.8. Thus, the external moment per unit length applied on the boring bar by the actuator force $F_a(f)$ may be approximated as [19]:

$$m_e(z, f) = \alpha F_a(f)(\delta(z - z_1) - \delta(z - z_2)) \quad (2.27)$$

where $\delta(z)$ is the Dirac delta function, z_1 and z_2 are the z -coordinates for the "boring bar - actuator" interfaces introduced by the DC-voltage offset required for the dynamic operation of the actuator and $z_2 - z_1 \approx L_a$ as $\max(\Delta L_a(t))/L_a \leq 0.2\%$ [40]. Expression of the Fourier Transform of Eq. 2.21 with Eq. 2.27 and integration of the resulting equation over the length of the boring bar yields the following expression for the generalized load of mode r :

$$F_{load,r}(f) = \alpha F_a(f)(\psi_r(z_2) - \psi_r(z_1)) \quad (2.28)$$

If $z_1 = 0$, one "boring bar - actuator" interface is at the clamped end, and the generalized load of mode r is given by:

$$F_{load,r}(f) = \alpha F_a(f)\psi_r(z_2) \quad (2.29)$$

Thus, the frequency-domain dynamic response of the boring bar in the y -direction may be expressed as [19]:

$$w(z, f) = \sum_{r=1}^{\infty} \psi_r(z) H_r(f) \alpha H_{fv}(f) V(f) \psi_r(z_2) \quad (2.30)$$

where $H_r(f)$ is the frequency response function for the mode r .

2.4 "3-D" Finite Element Model

A finite element model of the system "boring bar - actuator - clamping house" was built using the commercial finite element software MSC.MARC [41]. The initial "3-D" finite element model of the clamped boring bar includes separate models of a boring bar, a clamping house and a model of a piezoelectric actuator interacting by means of frictionless contact.

The spatial dynamic properties of the "boring bar - actuator - clamping house" system were calculated based on the general equation for the dynamic equilibrium of an undamped system, i.e.,

$$[\mathbf{M}]\{\ddot{\mathbf{w}}(t)\} + [\mathbf{K}]\{\mathbf{w}(t)\} = \{\mathbf{0}\}, \quad (2.31)$$

where $[\mathbf{M}]$ is the global $N_{fem} \times N_{fem}$ mass matrix of the system, $[\mathbf{K}]$ is the global $N_{fem} \times N_{fem}$ stiffness matrix of the system, $\mathbf{w}(t)$ is the space- and time-dependent $N_{fem} \times 1$ displacement vector and N_{fem} is the number of degrees-of-freedom of the finite element model. The modal analysis was conducted by using the Lanczos iterative method in the MSC.MARC software [41, 42]. The dynamic behavior of the system was also examined by means of transient and harmonic response simulations.

2.4.1 Model of the system "boring bar - clamping house"

The model of the system "boring bar - clamping house" consists of two sub-models: a sub-model of the boring bar and a sub-model of the clamping house. The sub-models are connected in terms of variable contact [41]. As a basic finite element, a tetrahedron was chosen.

The sub-model of the boring bar consists of three parts: the "body" which models the part of the boring bar with a constant cross-section, the "head" which models the part of the boring bar with a varying cross-section, and the "tool", which models the attached insert. In order to simplify the meshing process and keep down the number of degrees-of-freedom in the system while still maintaining accuracy within the model, the three boring bar parts were meshed separately with different element edge lengths (see Table 2.6). These three parts were connected using "glue" contact, which implies that the contacting nodes of both parts are tied to each other in such a way that there is no relative normal or tangential motion between the two parts in these nodes. The finite element model of the boring bar is shown in Fig. 2.9 a).

For the sake of simplicity, the clamping house and the four clamping screws were modeled as one body. The sub-model of the clamping house was built using four-noded tetrahedrons with linear shape functions. The element edge

Sub-model	Element Edge Length (m)	Polynomial order
Boring bar, "body"	0.01	2
Boring bar, "head"	0.005	2
Boring bar, "tool"	0.005	2
Clamping house	0.005-0.01	1
Actuator	0.01	1

Table 2.6: Finite element size and order of the approximation polynomial used in the shape functions.

length varies from 0.005 m to 0.01 m, depending on the location of the finite element in the model, i.e., surfaces of the clamping house that are in contact with the boring bar have a mesh with higher density than the rest of the clamping house surfaces. For the clamping house surfaces in contact with the turret, the following boundary conditions were used: nodal displacements on the surfaces of the clamping house, which correspond to surfaces of the real clamping house attached to the turret (see Fig. 2.4 b)) in x -, y - and z -directions are set to zero. The finite element model of the clamping house is shown in Fig. 2.9 b).

2.4.2 Model of the Actuator

A "3-D" finite model of a piezoelectric actuator was developed. Thin layers of an electrically active ceramic material connected in parallel were modeled as a stack of eight-noded bricks with piezoelectrical properties, i.e., in addition to three translational degrees-of-freedom, each node has a fourth degree-of-freedom - electric potential. The number of bricks or piezoelectric layers η_a can be calculated based on the formula for the free expansion of an unloaded stack actuator [38].

$$\Delta L_a = \eta_a d_{33} V(t) \quad (2.32)$$

where d_{33} is the actuator's strain coefficient, $V_{max}(t)$ is the max operating voltage and ΔL_a is the free expansion of the actuator. These values are given in Table 2.1. This yields $\eta_a = 400$ bricks or piezoelectric layers in the actuator stack.

The large number of layers affects the computational complexity of the finite element model. For this reason, it is desirable to have a model with a minimal number of degrees-of-freedom ensuring sufficient accuracy. The number of the piezoelectric layers was reduced with a factor of 10 and the strain

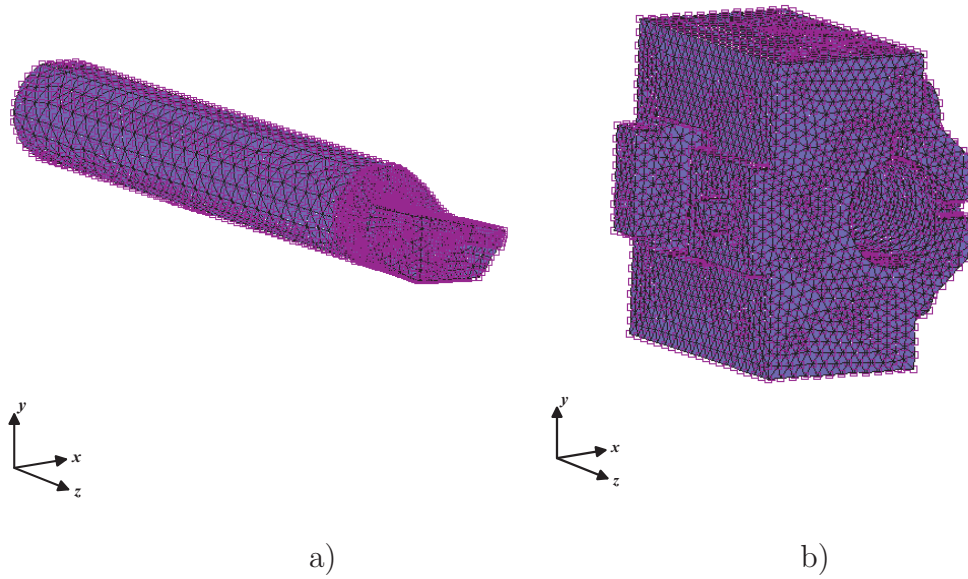


Figure 2.9: The 3-D finite element model of a) a boring bar and b) a clamping house.

constant d_{33} , which yields the specified free expansion ΔL_a , was increased with a factor of 10. Since the reduced number of layers is still large, i.e., 40 layers, only a principal sketch of the "3-D" finite element model of the actuator is shown in Fig. 2.10.

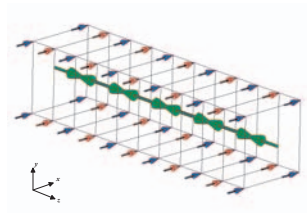


Figure 2.10: Sketch of a "3-D" finite element model of an actuator.

The electrostatic boundary conditions are shown in Fig. 2.10. The blue arrows show the nodes with applied negative or zero potential, and the red arrows correspond to the nodes with applied positive potential. Furthermore, the large green arrows show the material orientations within the finite elements. The material orientation in this case determines the direction of current flow

inside the finite element.

2.4.3 Contact Modeling in the Finite Element Analysis

The adequate modeling of the boring bar dynamic motion requires incorporation of the contact conditions between the boring bar, clamping house and clamping bolts into the "3-D" finite element model.

By a numerical contact problem, a complex process of the interaction of two or more numerical regions' boundaries may be defined in the computational domain based on constraints and boundary conditions specified by the physical nature of the contact between the bodies, e.g., friction or heat transfer [43].

Three objectives of the contact between the boring bar, clamping house and clamping screws may be stated:

- Detection of the contact between pre-defined contacting bodies;
- Application of constraints to avoid penetration;
- Application of boundary conditions to simulate frictional behavior.

The two basic types of contact bodies are implemented in MSC.MARC, [41]: deformable and rigid. Thus, there are two types of contact: a contact between deformable and deformable bodies and a contact between deformable and rigid bodies.

A "3-D" deformable body is described by the "3-D" finite elements, and the nodes on its external surfaces are defined as potential contact nodes. Their "3-D" faces form the outer surfaces and are considered as potential contact segments.

Rigid bodies are usually composed of the analytically defined "3-D" Non Uniform Rational Basis (NURBS) surfaces, which are treated as potential contact segments. Rigid bodies do not deform.

Contact tolerance

Conventionally, the contact between two "3-D" bodies is implemented in the following way: one body is determined to be the "master", and the other is determined to be the "slave" body [44].

The "master" body is always deformable. The contacting element of the "master" body is a node. The "slave" body can be deformable or rigid. The contacting element of the "slave" body is a segment which can be assembled by a patch of the "3-D" finite element faces in the case of a deformable body or segments in the case of a rigid body.

Deformable-rigid contact

In this case, contact between the deformable "master" body and the rigid "slave" body is considered.

In order to simplify the numerical implementation of the contact, contact tolerance was introduced to determine the distance below which bodies are considered to be in contact. For instance, node A in Fig. 2.11 is not inside the contact tolerance interval, thus the "master" and the "slave" bodies are not in contact. The contact tolerance in the MSC.MARC software is defined as 5 % of the smallest element edge length in the finite element model [41].

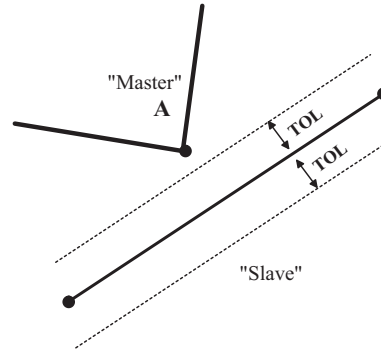


Figure 2.11: Contact tolerance.

Contact detection

If node A is within the contact tolerance interval, then the "master" and the "slave" bodies are considered to be in contact (see Fig. 2.12). In the MSC.MARC software, the contact problem is resolved by using the direct constraint method [41]. This implies that when contact is detected, the motion of the contacting bodies is constraint by means of boundary conditions, i.e., displacements and nodal forces are recalculated.

When variable contact occurs, the constraints are imposed on degrees-of-freedom of node A . The displacement of node A is transformed into the local coordinate system of the rigid body, which has as its basis the normal $\{\eta\}$ and tangential $\{\tau\}$ vectors. The relative displacement of node A is updated as follows:

$$\Delta\{\mathbf{w}\}_\eta = \{\mathbf{v}\}^T\{\eta\} \quad (2.33)$$

where $\{\mathbf{v}\}$ is the velocity vector of the rigid body. Thus in this case, the "master" and "slave" bodies move together with the same speed in the normal

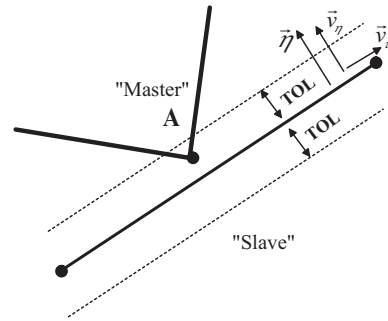


Figure 2.12: Contact detection.

direction, however the "master" body can slide on the surface of the "slave" body in the tangential direction.

In the case of the glue contact, additional constraint is imposed, such that no relative tangential motion occurs between the "master" and the "slave" body:

$$\Delta\{\mathbf{w}\}_\tau = \{\mathbf{v}\}^T \{\tau\} \quad (2.34)$$

Detection of penetration and separation

When the contacting node A moves beyond the contact tolerance interval, it is considered to be penetrating the "slave" body. In this case, the iterative penetration checking procedure is invoked [41].

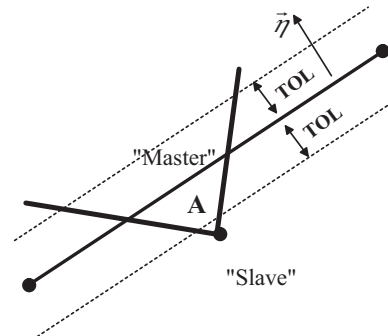


Figure 2.13: Penetration detection.

Application of Boundary Conditions - Direct Constraint method

In order to conduct contact analysis, different techniques can be utilized, e.g., the Lagrange multiplier procedure, the penalty method, hybrid and mixed methods, and the direct constraint method [41]. The direct constraint method provides an accurate solution for contact analysis [41]. The principle of the direct constraint method is enclosed in the application of constraints due to contact by means of boundary conditions, i.e., normal displacements and nodal forces.

The problem can be formulated as follows:

$$\begin{bmatrix} [\mathbf{K}_{aa}] & [\mathbf{K}_{ab}] \\ [\mathbf{K}_{ba}] & [\mathbf{K}_{bb}] \end{bmatrix} \begin{Bmatrix} \{\mathbf{w}_a\} \\ \{\mathbf{w}_b\} \end{Bmatrix} = \begin{Bmatrix} \{\mathbf{f}_a\} \\ \{\mathbf{f}_b\} \end{Bmatrix} + \begin{Bmatrix} \{\mathbf{0}\} \\ \{\mathbf{f}_c\} \end{Bmatrix} \quad (2.35)$$

where subscript b is used for the transformed degrees-of-freedom associated with the nodes in contact, and subscript a is used for the other not transformed degrees-of-freedom; $[\mathbf{K}_{aa}]$ is a sub-matrix of the global stiffness matrix which corresponds to the degrees-of-freedom of nodes which are not in contact; $[\mathbf{K}_{bb}]$ is a sub-matrix of the global stiffness matrix which corresponds to the degrees-of-freedom associated with nodes in contact; $[\mathbf{K}_{ab}]$ and $[\mathbf{K}_{ba}]$ are sub-matrices of the global stiffness matrix which corresponds to the degrees-of-freedom of nodes in contact respective non-contacting nodes; $\{\mathbf{w}_a\}$ is the space- and time-dependent vector of unknown displacements associated with non-contacting nodes; $\{\mathbf{w}_b\}$ is the space- and time-dependent vector of constrained displacements; $\{\mathbf{f}_a\}$ and $\{\mathbf{f}_b\}$ are space- and time-dependent vectors of external forces acting on the constrained and unconstrained degrees-of-freedom respectively and $\{\mathbf{f}_c\}$ is the space and time dependent vector of unknown contact forces. The unknown displacements and contact forces can be found by means of Gaussian elimination as follows [44]:

$$[\mathbf{K}^*]\{\mathbf{w}_b\} - \{\mathbf{f}_c\} = \{\mathbf{f}^*\} \quad (2.36)$$

where $[\mathbf{K}^*]$ and $\{\mathbf{f}^*\}$ can be expressed as [44]:

$$[\mathbf{K}^*] = [\mathbf{K}_{bb}] - [\mathbf{K}_{ba}][\mathbf{K}_{aa}]^{-1}[\mathbf{K}_{ba}]^T \quad (2.37)$$

$$\{\mathbf{f}^*\} = \{\mathbf{f}_b\} - [\mathbf{K}_{ba}][\mathbf{K}_{aa}]^{-1}\{\mathbf{f}_a\} \quad (2.38)$$

where $[\mathbf{K}^*]$ is the $(N_{dof} \cdot n_c) \times (N_{dof} \cdot n_c)$ stiffness matrix, N_{dof} is the number of degrees-of-freedom at the node of the finite element (in the case of a 10-noded tetrahedron, $N_{dof} = 3$), n_c is the number of contacting nodes. The vectors $\{\mathbf{f}^*\}$, $\{\mathbf{f}_c\}$, $\{\mathbf{w}_b\}$ have a length of $N_{dof} \cdot n_c$. Thus, the system of linear

equations Eq. 2.36 has $2 \cdot N_{dof} \cdot n_c$ unknown and only $N_{dof} \cdot n_c$ equations. In order to obtain a unique solution of the system to linear equation Eq. 2.36, one has to complete this system by using additional conditions, e.g., conditions of compatibility and equilibrium [44].

Compatibility condition The compatibility condition implies, that when contact is detected within the contact tolerance, two bodies start to move together, i.e., Eq. 2.33 is used in the case of variable contact, and Eq. 2.33 and Eq. 2.34 are utilized in the case of glue contact.

Equilibrium condition The contact forces between the contacting node of the "master" body $\{\mathbf{f}_m\}$ and the contacting segment of the "slave" body $\{\mathbf{f}_{sl}\}$ should be equal and opposite, yielding:

$$\{\mathbf{f}_m\} + \{\mathbf{f}_s\} = 0 \quad (2.39)$$

For the glue contact, additional condition is applied:

$$\{\mathbf{f}_m\}^T \{\tau\} = \{\mathbf{f}_{sl}\}^T \{\tau\} = 0 \quad (2.40)$$

Deformable-deformable contact

In the case of contact between two deformable bodies, the multi-point constraint is imposed on the contacting node. This means that for each contacting node, the retained nodes are found from the set of boundary nodes, e.g., for the 10-noded tetrahedrons, the number of retained nodes is seven - six from the patch plus the contacting node itself. Retained nodes are used to form a geometrical surface. After a normal vector $\{\eta\}$ to this surface is found, the analysis proceeds as in the case of the deformable-rigid contact. In the case of a deformable-deformable contact, there is no "master"- "slave" relationships; each contacting body is checked against every other body.

2.4.4 Coulomb Friction Modeling

Generally, the dynamic response of the boring bar during a continuous turning operation has nonlinear properties [33, 34]. Possible sources of nonlinearities are, for instance, the intermittent contact between the workpiece and the cutting tool, as well as a nonlinear contact between the boring bar, clamping screws and the inner surface of the clamping house cavity [33, 34]. Only the second source of nonlinearities is considered in the present study. However, the incorporation of a cutting process model is of great importance for further

research. When the boring bar is excited by the force originated from the material deformation process, relative motion between the contacting surfaces of the boring bar, clamping screws and clamping house occurs. Thus, it is likely that some of the energy introduced into the system by the cutting process dissipates via friction forces at contacting surfaces between the boring bar and clamping house [45]. Generally, no lubricating film is used between the boring bar and clamping house surfaces. Such contact may be considered as a dry frictional contact. Therefore, the Coulomb model of the friction force may be used (see Fig. 2.14). The model implies that for relative motion between contact surfaces, the static friction force f_{st} , which is greater than kinetic friction force f_k (due to the difference between the static and kinetic friction coefficients $\mu_k < \mu_{st}$), should be overcome. Thus, the stick-slip friction force can be expressed as follows [41]:

$$f = \begin{cases} |f_{st}| = \mu_{st}f_n, & \{\mathbf{v}\} = 0 \\ f_k = -\mu_k f_n \text{sign}(\{\mathbf{v}\}), & \text{otherwise} \end{cases} \quad (2.41)$$

where f_n - is a normal force acting on surface or body and $\{\mathbf{v}\}$ is the relative sliding velocity vector.

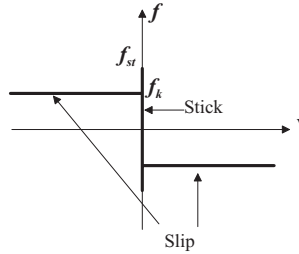


Figure 2.14: Coulomb model of dry friction force.

As the result of the dry friction force presence in the system, the relative motion of contacting surfaces or bodies can be considered as a stick-slip oscillation. Thus, it may affect the dynamic properties of the system "boring bar - clamping house". The friction coefficients μ_k and μ_s are usually determined experimentally. As a kinetic friction coefficient, $\mu_k = 0.4$ which corresponds to the typical friction coefficient of unlubricated materials such as chromium hard steel at low speeds in normal atmospheres against a mild steel counterface [45].

Two different Coulomb friction force model approximations were incorporated into the "3-D" finite element model of the system "boring bar - actuator - clamping house": the arctangent model and the bilinear model.

Arctangent model

This model approximates a discontinuous Coulomb friction force function by a continuously differentiable function of the relative sliding velocity (see Fig. 2.16) [41].

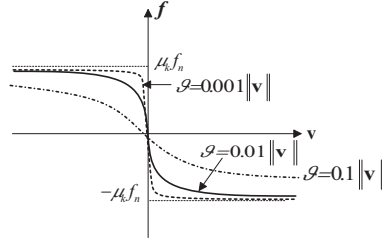


Figure 2.15: Arctangent approximation for the Coulomb friction model.

Thus, the friction force is described by [41]:

$$f = -\mu_k f_n \frac{2}{\pi} \tan^{-1} \left(\frac{\|\{\mathbf{v}\}\|}{\vartheta} \right) \text{sign}(\{\mathbf{v}\}) \quad (2.42)$$

where ϑ - is a value of relative velocity below which sticking occurs. It is expressed as a percentage of the maximum relative sliding velocity v_{max} and usually is taken from the interval $\vartheta \in [0.01v_{max}, 0.1v_{max}]$. Small values of ϑ yield a narrow stick velocity interval, i.e., a closer approximation of the Coulomb friction model. This also implies that sticking will occur only at very low velocities, and the slipping mode will be dominant. On the other hand, large values of ϑ may result in insufficient influence of the friction in the boring bar model. One way to obtain the initial value of ϑ might be to estimate it based on transient analysis without incorporated friction force.

Bilinear model

This model is based on relative displacement instead of relative velocity. It describes a sticking behavior in terms of elastic relative displacements and a slipping mode in terms of plastic relative displacements [41].

The friction force can be expressed as [41]:

$$f = \begin{cases} -\frac{\mu_k f_n}{\delta} \Delta\{\mathbf{w}\}, & |\Delta\{\mathbf{w}\}| < \delta \\ -\mu_k f_n \text{sign}(\Delta\{\mathbf{w}\}), & \text{otherwise} \end{cases} \quad (2.43)$$

where δ is the slip threshold or relative sliding displacement below which the sticking is simulated. The default value of δ is calculated in MSC.MARC as

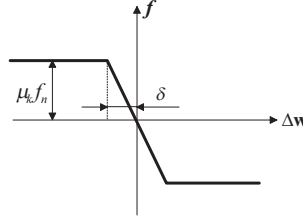


Figure 2.16: Bilinear approximation for the Coulomb friction model.

$0.0025 \times \bar{l}_e$, where \bar{l}_e is the average edge length of the finite elements defining the contacting bodies [41]. According to the theory of tribology, the dimension of a single contacting spot on an engineering surface is in the order of 10^{-5} m, which can be assumed as a typical amplitude for the stick-slip oscillation [45].

2.4.5 Transient response

Transient response simulation was conducted with the help of MSC.MARC software using the direct integration Single-Step Houbolt method [41]. This algorithm is recommended for nonlinear contact analysis due to its unconditional stability and second-order accuracy. A detailed description of this method can be found in [46]. The Single-Step Houbolt method uses a constant time step, which is convenient for the calculation of the response signal synchronized with the excitation signal.

The approximation of the system's equation of motion Eq. 2.13 by single-step algorithms in general form can be expressed as [46]:

$$\alpha_{m1}[\mathbf{M}]\{\mathbf{a}\}_{n+1} + \alpha_{c1}[\mathbf{C}]\{\mathbf{v}\}_{n+1} + \alpha_{k1}[\mathbf{K}]\{\mathbf{d}\}_{n+1} + \alpha_m[\mathbf{M}]\{\mathbf{a}\}_n + \alpha_c[\mathbf{C}]\{\mathbf{v}\}_n + \alpha_{k1}[\mathbf{K}]\{\mathbf{d}\}_n = \alpha_{f1}\{\mathbf{f}\}_{n+1} + \alpha_f\{\mathbf{f}\}_n \quad (2.44)$$

$$\{\mathbf{d}\}_{n+1} = \{\mathbf{d}\}_n + \Delta t \dot{\mathbf{d}}_n + \beta \Delta t^2 \ddot{\mathbf{a}}_n + \beta_1 \Delta t^2 \ddot{\mathbf{a}}_{n+1} \quad (2.45)$$

$$\{\mathbf{v}\}_{n+1} = \{\mathbf{v}\}_n + \gamma \Delta t \dot{\mathbf{a}}_n + \gamma_1 \Delta t \dot{\mathbf{a}}_{n+1} \quad (2.46)$$

where $\{\mathbf{a}\}_n$, $\{\mathbf{v}\}_n$ and $\{\mathbf{d}\}_n$ are the approximations of $\{\ddot{\mathbf{w}}(t_n)\}$, $\{\dot{\mathbf{w}}(t_n)\}$, $\{\mathbf{w}(t_n)\}$ respectively, Δt is a step size and α_{m1} , α_{c1} , α_{k1} , α_m , α_c , α_{k1} , α_{f1} , α_f , β_1 , β , γ_1 , γ are the algorithmic parameters. The algorithmic parameters may be tuned by means of conditions of asymptotic annihilation and second-order accuracy, as well as by certain overshoot behavior imposed on the response calculated by the algorithm [46].

According to [46], the algorithm begins with calculation of

$$\{\mathbf{a}\}_0 = [\mathbf{M}]^{-1} (\{\mathbf{f}_0\} - [\mathbf{C}]\{\mathbf{v}_0\} - [\mathbf{K}]\{\mathbf{d}_0\}) \quad (2.47)$$

2.4.6 Harmonic response

The harmonic response of the "3-D" finite element model of the system "boring bar - actuator - clamping house" was calculated with the use of MSC.MARC software. In general, the solution process is based on the Fourier Transform of the equation motion of the damped system Eq. 2.13.

$$((j2\pi f)^2[\mathbf{M}] + (j2\pi f)[\mathbf{C}] + [\mathbf{K}])\{\mathbf{W}(f)\} = \{\mathbf{F}(f)\} \quad (2.48)$$

The excitation force $\{\mathbf{F}\} = \{\mathbf{f}\}e^{j2\pi f}$ in this case is assumed to have a constant magnitude at all frequencies. Then, the displacement vector $\{\mathbf{W}\}$ is found by solving Eq. 2.48 for each frequency from the specified frequency range. Thus, the receptance frequency response function is found as a ratio of displacement $\{\mathbf{W}(f)\}$ and force $\{\mathbf{F}(f)\}$ vectors.

$$\{\mathbf{W}(f)\} = ((j2\pi f)^2[\mathbf{M}] + (j2\pi f)[\mathbf{C}] + [\mathbf{K}])^{-1}\{\mathbf{F}(f)\} \quad (2.49)$$

$$[H_r(f)] = \frac{\{\mathbf{W}(f)\}}{\{\mathbf{F}(f)\}} = ((j2\pi f)^2[\mathbf{M}] + (j2\pi f)[\mathbf{C}] + [\mathbf{K}])^{-1} \quad (2.50)$$

The damping in this case is assumed to be proportional, i.e., $[\mathbf{C}] = \alpha[\mathbf{M}] + \beta[\mathbf{K}]$, where the coefficients α and β are chosen such that relative damping ratios at the, for instance, two lowest eigenfrequencies correspond to the relative damping values estimated by experimental modal analysis. This condition can be expressed as follows [36]:

$$\zeta_r = \frac{\alpha}{4\pi f_r} + \beta\pi f_r \quad (2.51)$$

where f_r , $r = 1, 2, \dots, N_{ema}$ is the r th natural frequency.

One disadvantage of this approach is that the variable contact between the clamping house and the boring bar is disregarded.

2.5 SDOF Nonlinear Model

In order to investigate effects of the arctangent and bilinear approximations of the Coulomb friction force on the dynamics of a clamped boring bar, the simplest case when the boring bar is described by a SDOF model was considered.

The response of the boring bar during an internal turning operation in the lathe is usually dominated by the fundamental bending mode in the cutting speed direction [4, 3]. Therefore, a simple SDOF model with mass m , stiffness k and damping c corresponding to the modal mass, stiffness and damping of the respective fundamental bending mode is considered.

A simple SDOF system with nonlinear friction force included, described by the arctangent model, may be described by the following equation of motion [41]:

$$m\ddot{w}(t) + c\dot{w}(t) + kw(t) + \mu_k mg \frac{2}{\pi} \tan^{-1} \left(\frac{\dot{w}(t)}{\vartheta} \right) = f(t) \quad (2.52)$$

where $f(t)$ is the excitation force.

On the other hand, if the nonlinear friction force is approximated by the bilinear model, the equation of motion of the SDOF system is as follows:

$$m\ddot{w}(t) + c\dot{w}(t) + kw(t) + \mu_k mg w(t) = f(t), \quad \text{if } w(t) > \delta \quad (2.53)$$

$$m\ddot{w}(t) + c\dot{w}(t) + kw(t) + \frac{\mu_k mg}{\delta} w(t) = f(t), \quad \text{otherwise} \quad (2.54)$$

The response of the SDOF system under random excitation force was calculated in Matlab with the help of the Runge-Kutta method, the ode45 solver [47]. The response of the SDOF system was calculated for the range of parameters ϑ and δ , as well as for a set of excitation force levels. The frequency response functions between the excitation force and the acceleration of the SDOF system were estimated in order to facilitate the interpretation of results obtained based on the "3-D" FE model.

Chapter 3

Results

The results are presented in the following order: firstly, the estimates of the two fundamental natural frequencies and the corresponding mode shapes based on experimental modal analysis and the linear "3-D" FE-model are given. Secondly, the results of the system identification in terms of the frequency response functions of the so called control path, the accelerances between the actuator voltage and the acceleration measured by error accelerometers (accelerometers attached close to the tool tip) both in the cutting speed and cutting depth directions are presented. Here, experimental modal analysis of the active boring bar, simulation of the harmonic response of the active boring bar finite element model with linear clamping conditions, and simulation of the transient response of the active boring bar finite element model enabling variable contact between the boring bar and the clamping house were utilized. Thirdly, frequency response function estimates for the dynamic response of the control paths of the "3-D" FE-model enabling variable contact between the boring bar and the clamping house with nonlinear Coulomb friction force between the contacting surfaces of the boring bar, clamping screws and clamping house are given. Here, results of two different Coulomb friction force models' influences on the dynamic response of a SDOF system in terms of frequency response function estimates are reported first. This is done in order to facilitate the interpretation of the frequency response function estimates of the dynamic response of the control paths of the active boring bar "3-D" FE-model with the Coulomb friction force and enabling clamping house variable contact. The control path accelerance functions are calculated for a range of values of the governing parameter in both the arctangent and bilinear models. Fourthly, receptance function estimates between the force produced by the actuator and the displacement of the "boring bar - actuator" interfaces obtained based on the simulated transient response of the active boring bar finite element model enabling variable contact between the boring bar and clamping

house are given. Finally, frequency response function estimates between the actuator voltage and the strain at four different positions in the axial direction close to the "boring bar - actuator" interfaces for both FE model with variable contact and the actual boring bar are discussed.

3.1 Modal Analysis Results

3.1.1 Natural Frequencies

The two fundamental natural frequencies for the active boring bar estimated by experimental modal analysis and calculated based on the linear "3-D" finite element model are given in Table 3.1.

Model	Mode 1		Mode 2	
	Frequency, [Hz]	Damping ratio, [%]	Frequency, [Hz]	Damping ratio, [%]
Experimental Modal Analysis, (EMA)	501.638	1.044	520.852	1.244
"3-D" FEM of the active boring bar, (FEM)	496.232	-	529.046	-

Table 3.1: Two fundamental natural frequencies and corresponding damping ratios estimates.

3.1.2 Mode Shapes

The mode shapes estimated using experimental modal analysis and calculated based on the "3-D" finite element model of the system "boring bar - actuator - clamping house" are plotted in Fig. 3.1.

As a quality measure of the mode shapes extracted by experimental modal analysis, the MAC-matrix was calculated based on Eq. 2.16 [32], yielding:

$$\begin{aligned}
 [MAC]_1 &= \begin{bmatrix} MAC_{EMA_1,EMA_1} & MAC_{EMA_1,EMA_2} \\ MAC_{EMA_2,EMA_1} & MAC_{EMA_2,EMA_2} \end{bmatrix} = \quad (3.1) \\
 &= \begin{bmatrix} 1.000 & 0.000 \\ 0.000 & 1.000 \end{bmatrix}
 \end{aligned}$$

where EMA_1 is the mode shape at 501.638 Hz, and EMA_2 is the mode shape at 520.852 Hz.

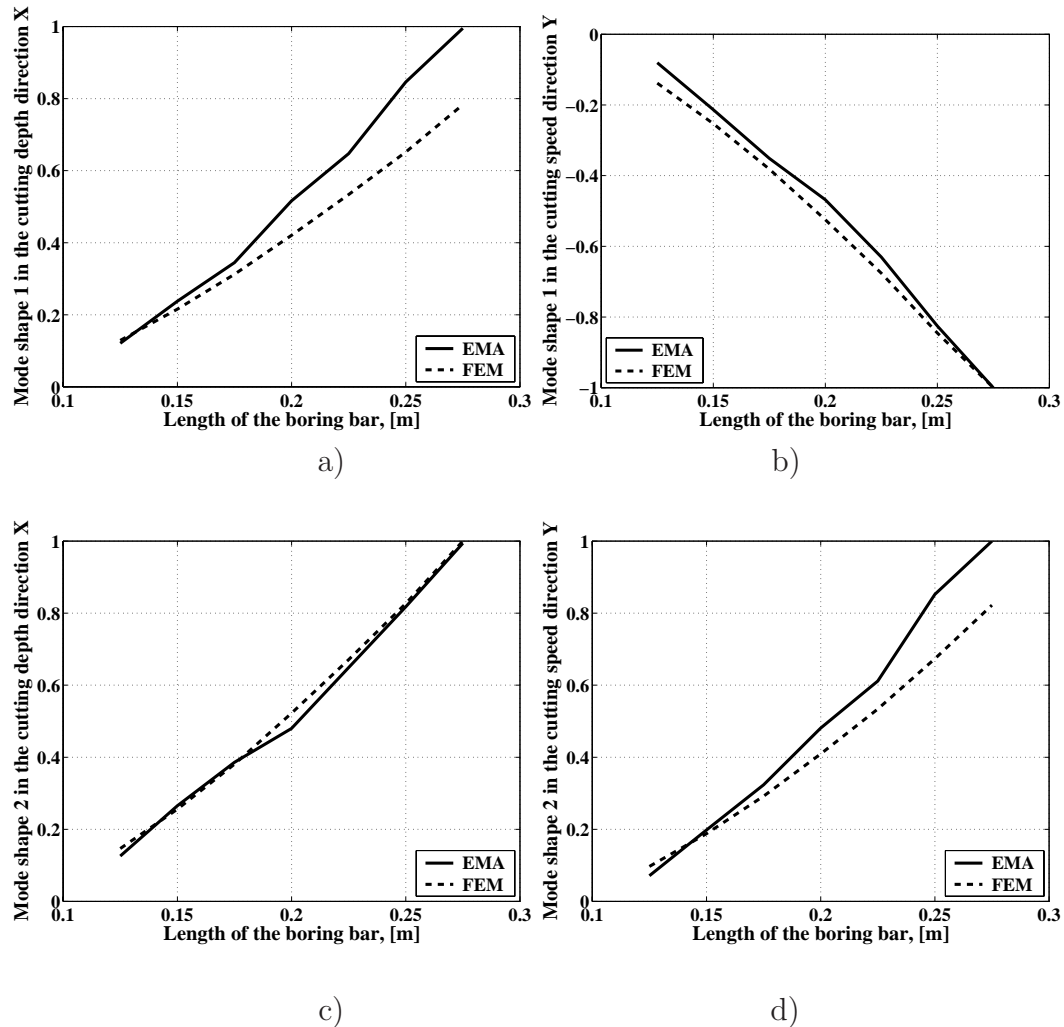


Figure 3.1: The first two fundamental mode shapes of the active boring bar: a) component of mode shape 1 in the cutting depth direction, b) component of mode shape 1 in the cutting speed direction, c) component of mode shape 2 in the cutting depth direction and d) component of mode shape 2 in the cutting speed direction (estimated with experimental modal analysis (EMA) and finite element model (FEM)).

To provide a quantitative measure on the correlation between the mode shapes from the experimental modal analysis and the mode shapes predicted by the finite element models, a cross-MAC matrix has been produced based on Eq. 2.17 [32]. The cross-MAC matrix between the mode shapes calculated using the "3-D" finite element model FEM_1 at 496.232 Hz and FEM_2 at 529.046 Hz and mode shapes estimated using experimental modal analysis

EMA_1 at 501.638 Hz and EMA_2 at 520.852 Hz is given by:

$$\begin{aligned} [MAC]_2 &= \begin{bmatrix} MAC_{FEM_1,EMA_1} & MAC_{FEM_2,EMA_1} \\ MAC_{FEM_1,EMA_2} & MAC_{FEM_2,EMA_2} \end{bmatrix} = \\ &= \begin{bmatrix} 0.981 & 0.015 \\ 0.019 & 0.983 \end{bmatrix} \end{aligned} \quad (3.2)$$

3.2 System Identification

This section addresses system identification of two active boring bar transfer paths or control paths. The two transfer paths are as follows: one between the actuator voltage and the output signal from the accelerometer measuring the boring bar vibration in the cutting speed direction close to the insert, and the other one between the actuator voltage and the output signal from the accelerometer measuring the boring bar vibration in the cutting depth direction close to the insert, see Fig. 2.6. These control paths are estimated for both the actual active boring bar and for the FE models of the active boring bar.

3.2.1 Experimentally Estimated Accelerance

Two accelerance functions for the active boring bar were estimated: one between the actuator input voltage and the error accelerometer in the cutting speed direction and one between the actuator input voltage and the error accelerometer in the cutting depth direction. The spectrum estimation parameters and the excitation signal properties are given in Table 2.2. The magnitude function for the two estimated accelerance functions for the active boring bar are presented in Fig. 3.2.

3.2.2 Harmonic Response Based on FEM

The harmonic response was simulated using the linear "3-D" finite element model of the active boring bar. The results of the harmonic analysis are presented as the magnitude of two accelerance functions between the actuator voltage and the acceleration (error acceleration) at the two positions corresponding to the error accelerometer positions at the actual boring bar (see Fig. 3.3). The peak value of the amplitude of the harmonic excitation was equal to 100 V.

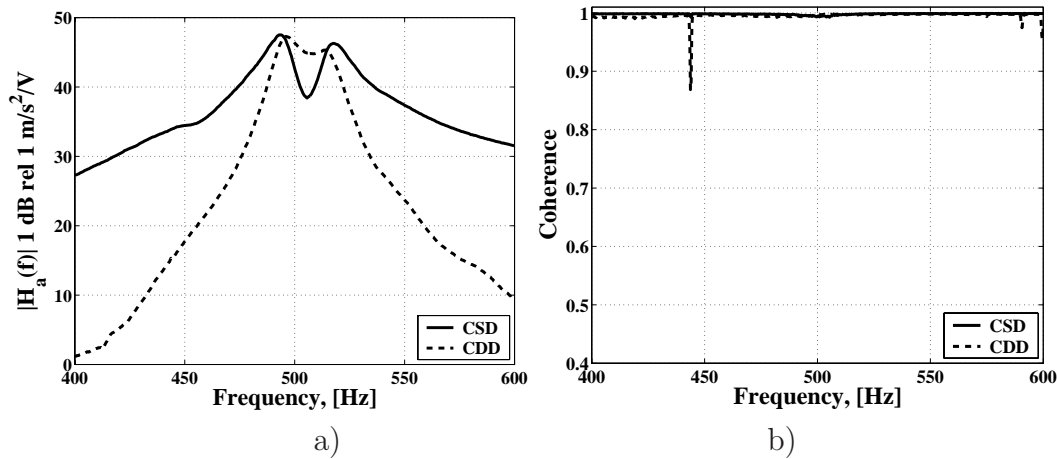


Figure 3.2: Magnitude of acceleration function estimates, between the actuator voltage and the error accelerometer in the cutting speed (CSD) direction and between the actuator voltage and the error accelerometer in the cutting depth (CDD) directions, and b) corresponding coherence functions estimates.

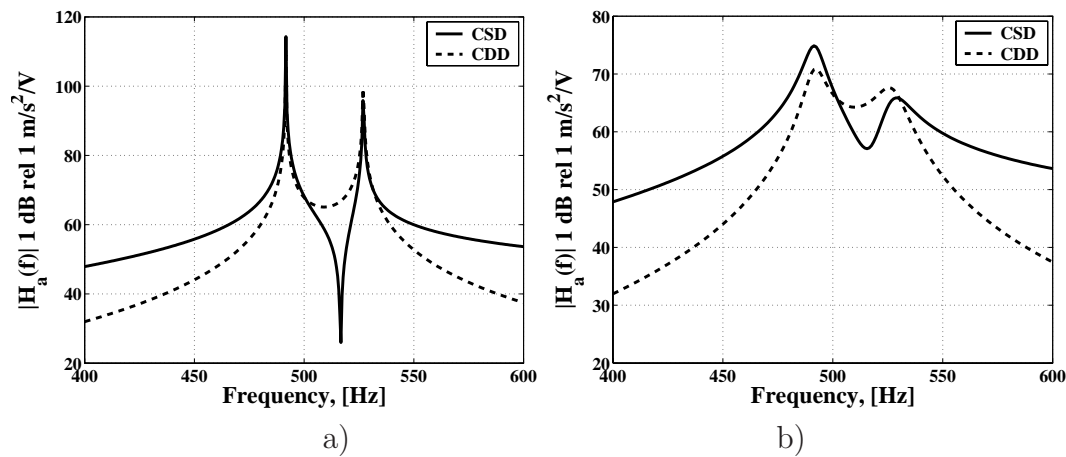


Figure 3.3: Magnitude of the acceleration function estimates, between the actuator voltage and the error acceleration in the cutting speed direction (CSD) and between the actuator voltage and the error acceleration in the cutting depth direction (CDD), based on the harmonic analysis of the "3-D" finite element model of the active boring bar: a) without damping, and b) with damping in the model.

3.2.3 Transient Response Based on FEM

The transient response of the "3-D" finite element model, enabling variable contact between the boring bar and the clamping house, was simulated with the use of the MSC.MARC software by means of the Single-Step Houbolt transient operator [41]. A uniformly distributed random excitation signal with a flat spectrum with an RMS value of 54.628 V was applied to the finite element model of the actuator. The results of the transient response simulation are presented as magnitude functions of accelerances between the actuator voltage and the acceleration at the points corresponding to the error sensor positions at the actual active boring bar in the cutting speed and cutting depth direction correspondingly (see Fig. 3.4).

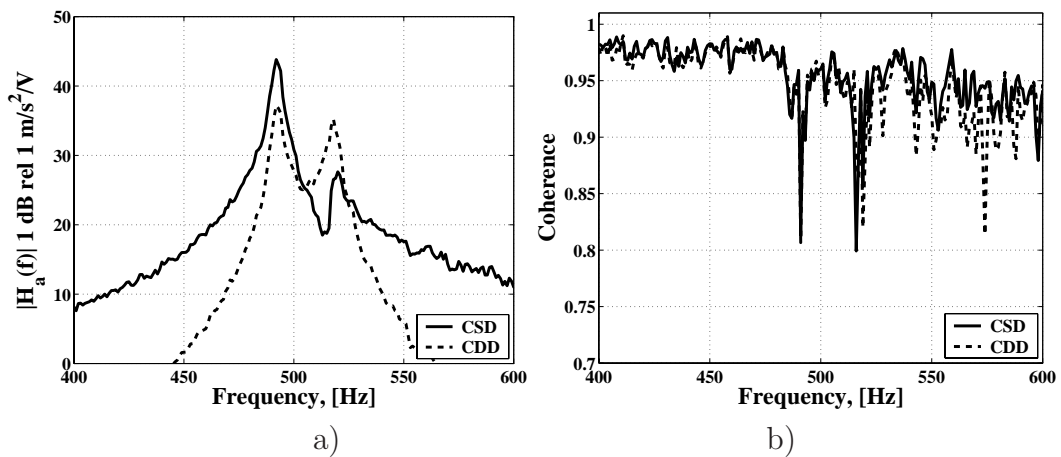


Figure 3.4: Magnitude of accelerance function estimates between the actuator voltage and the acceleration at the error sensor positions in the cutting speed (CSD), and in the cutting depth (CDD) directions, and b) corresponding coherence functions. Transient analysis of the "3-D" finite element model of the active boring bar enabling variable contact between the boring bar and the clamping house.

An estimated random error for the accelerance function estimate produced based on the "3-D" finite element model is shown in Fig. 3.5. The random error for the accelerance function estimate between the actuator voltage and the error accelerometer in cutting speed direction at the resonance frequencies is 0.072 and 0.063. The random error for the accelerance function estimate between the actuator voltage and the error accelerometer in cutting depth direction at the resonance frequencies is 0.070 and 0.061 respectively.

The magnitude functions of control path accelerance functions estimated

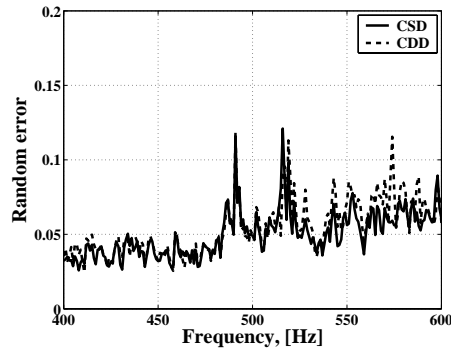


Figure 3.5: Random error for the accelerances estimated based on the "3-D" finite element model enabling variable contact between the boring bar and the clamping house.

experimentally and based on the simulation of the harmonic response of the linear "3-D" FE model and the transient response of the "3-D" FE model enabling variable contact between the boring bar and the clamping house are plotted together in the same diagram in Fig. 3.6.

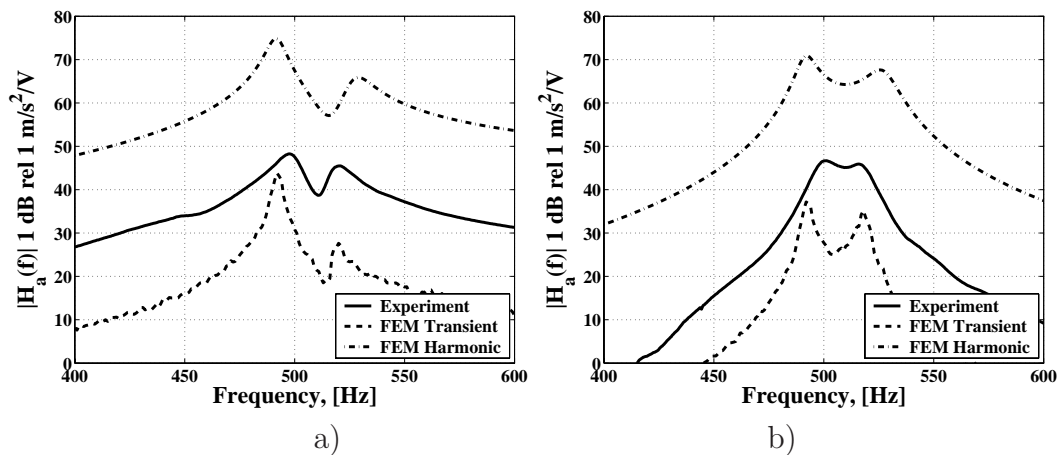


Figure 3.6: Magnitude of acceleration function estimates between the actuator voltage and the acceleration at the error sensor positions a) in the cutting speed (CSD), and b) in the cutting depth (CDD) directions obtained experimentally based on the simulation of the transient response and the harmonic response of the "3-D" finite element model of the active boring bar.

3.3 Dynamic Modeling of the Boring Bar with the Coulomb Friction Force Included

In order to improve the control path acceleration functions estimated based on the "3-D" finite element model enabling variable contact between the boring bar and the clamping house, the Coulomb friction force was included in the model. Two approximations of the Coulomb friction force were utilized: the arctangent and the bilinear. Dynamic motion of the boring bar excited by the actuator expansion results in the complex phenomenon of a variable contact between the boring bar and the clamping house. In order to investigate the influence of the Coulomb friction force on the dynamic behavior of the boring bar, acceleration functions were first calculated based on the simplest SDOF model of the boring bar for a range of values of the governing parameters and several excitation force levels. Then, the control path accelerances were calculated based on the "3-D" finite element model enabling variable contact between the boring bar and the clamping house for both the arctangent and the bilinear approximations of the Coulomb friction force. In this case, simulations of the transient response of the boring bar were carried out for the limited range of values of the governing parameters (for both the arctangent and the bilinear model) and a single excitation force level due to the long computational time required for each simulation.

3.3.1 Transient Response Based on the SDOF Model

In order to simulate the nonlinear SDOF system described by Eq. 2.52 or Eq. 2.53 and Eq. 2.54, the mass m , stiffness k and damping c have to be selected. For the sake of relevance, these quantities are estimated based on the driving point acceleration function estimate for the cutting speed direction produced in the experimental modal analysis of the active boring bar (see Fig. 3.7).

The modal parameters m , k and c can now be estimated based on the following expressions:

$$k = \frac{2\pi^2 f_n^2}{\zeta_n |H_a(f_n)|} \quad (3.3)$$

$$m = \frac{k}{(2\pi f_n)^2} \quad (3.4)$$

$$c = 2\zeta_n \sqrt{mk} \quad (3.5)$$

where f_n is the undamped fundamental natural frequency in the cutting speed direction, ζ_n is the corresponding damping ratio, $|H_a(f_n)|$ is the value of the

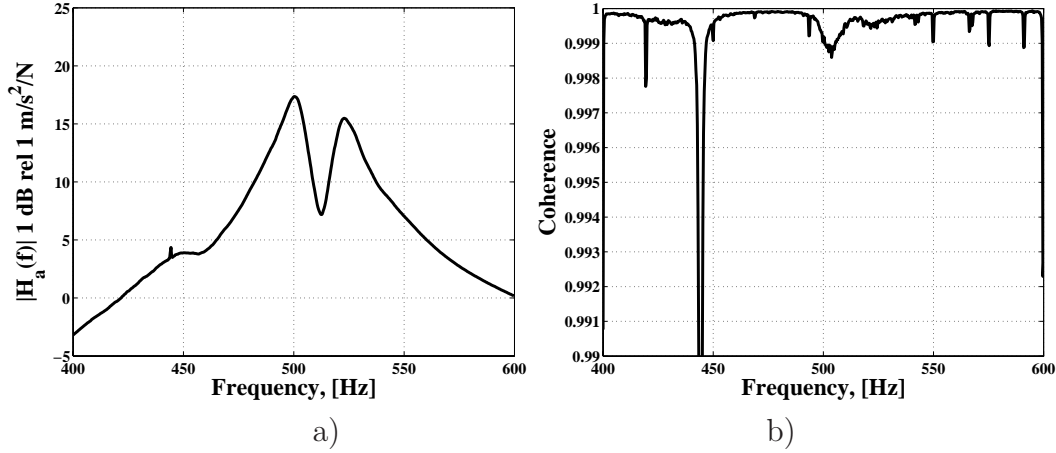


Figure 3.7: Magnitude of driving point accelerance estimate for the boring bar in the cutting speed direction (CSD), and b) corresponding coherence function (produced in experimental modal analysis).

magnitude function of the driving point accelerance function estimate in the cutting speed direction at the fundamental natural frequency in the cutting speed direction.

The estimated values of the modal mass, stiffness and damping are as follows: $m = 6.489$ [kg], $k = 64.467 \times 10^6$ [N/m] and $c = 427.071$ [Ns/m]. These mass, stiffness and damping values were used in the simulations of the response of the SDOF model with the arctangent and bilinear approximations of the nonlinear friction force for uniformly distributed broadband random force with RMS levels of 57.827 N, 289.088 N, 576.647 N, 2888.338 N and 5762.465 N.

The response of the SDOF model with the arctangent approximation of the Coulomb friction force was calculated for the following parameters of the relative sliding velocity:

$$\vartheta = [0.005\dot{w}_{max} \quad 0.01\dot{w}_{max} \quad 0.05\dot{w}_{max} \quad 0.1\dot{w}_{max}] \quad (3.6)$$

where \dot{w}_{max} is the maximum velocity estimated based on the linear model. The relative damping ratios estimated for each value of parameter ϑ at each excitation force level are summarized in Table 3.2.

The magnitude function for the accelerance function estimates between the uniformly distributed random force with an RMS level of 576.647 N and the acceleration of the SDOF model calculated for the range of values of the parameter ϑ together with corresponding coherence functions are shown in Fig. 3.8.

Excitation force RMS level, [N]	Damping ratio, [%]			
	$0.005\dot{w}_{max}$	$0.01\dot{w}_{max}$	$0.05\dot{w}_{max}$	$0.1\dot{w}_{max}$
57.827	72.447	68.034	29.007	17.136
289.088	4.572	4.572	4.175	3.746
576.647	3.047	3.047	2.847	2.624
2888.338	1.994	1.994	1.944	1.944
5762.465	1.844	1.844	1.894	1.894

Table 3.2: Estimates of the relative damping for the frequency response functions based on the SDOF nonlinear model with the arctangent approximation of the Coulomb friction force.

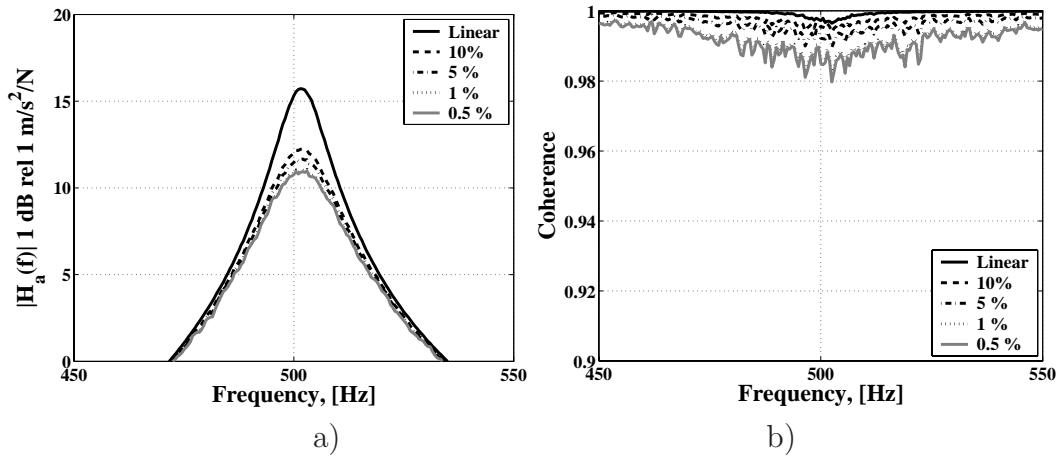


Figure 3.8: a) Magnitude of acceleration functions calculated based on the response of the SDOF model with the arctangent approximation of nonlinear force for the different values of the relative velocity ϑ and b) corresponding coherence functions (excitation force RMS level 576.647 N).

The response of the SDOF model with the bilinear approximation of the Coulomb friction force was calculated for the following values of the slip threshold δ : 10^{-6} [m], $5 \cdot 10^{-6}$ [m], 10^{-5} [m], $5 \cdot 10^{-5}$ [m] and 10^{-4} [m]. Natural frequency estimates for each of the combinations of δ and the excitation force levels are given in Table 3.3.

The magnitude function for the acceleration function estimates between the uniformly distributed random force with an RMS level of 576.647 N and the acceleration of the SDOF model calculated for the range of values of the parameter δ together with corresponding coherence functions are shown in Fig.

Excitation force RMS level, [N]	Natural frequency, [Hz]				
	$\delta = 10^{-4}$, [m]	$\delta = 5 \cdot 10^{-5}$, [m]	$\delta = 10^{-5}$, [m]	$\delta = 5 \cdot 10^{-6}$, [m]	$\delta = 10^{-6}$, [m]
57.827	502.5	504	511.5	520	549
289.088	502.5	504	508	511.5	537.5
576.647	502.5	504	507	510	535
2888.338	502.5	502.5	505.5	509.5	532.5
5762.645	502.5	502.5	505	509.5	532.5

Table 3.3: Estimates of the natural frequency for the frequency response functions based on the SDOF nonlinear model with the bilinear approximation of the Coulomb friction force.

3.9.

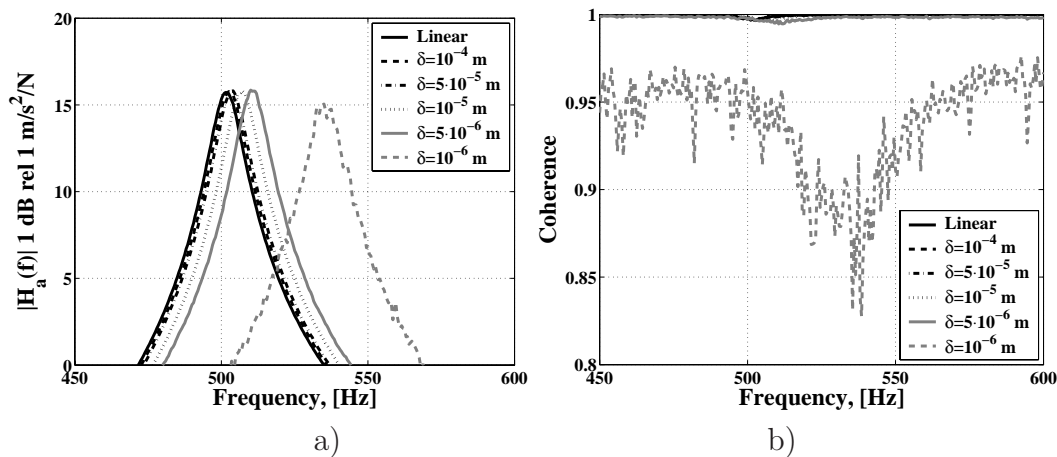


Figure 3.9: a) Magnitude of accelerances calculated based on the response of the SDOF model with bilinear approximation of nonlinear force for the different values of the slip threshold δ and b) corresponding coherence function (excitation force RMS level 576.647 N).

3.3.2 Dynamics of the "3-D" Finite Element Model Enabling Variable Contact between the Boring Bar and the Clamping House and also with Coulomb Friction Force

The initial value of the relative sliding velocity v was estimated based on the transient analysis of the finite element model enabling variable contact between the boring bar and the clamping house while allowing for no friction. The maximum velocity in the feed direction of the nodes of the boring bar finite element model corresponding to the bolts clamping position on the boring bar was $\dot{w}_{max} = 0.007784$ [m/s]. The arctangent friction model was tested for four different percentage values of the maximum sliding velocity: 10%, 5%, 1% and 0.5 %. The accelerance functions between the actuator voltage and the accelerations at the point of the active boring bar error sensor positions were estimated based on the transient analysis of the "3-D" finite element model with the arctangent friction model enabling variable contact between the clamping house and the boring bar for the four different relative sliding velocities. Magnitude functions for these accelerance functions are plotted together with the corresponding accelerance function for the finite element model enabling variable contact between the boring bar and the clamping house while allowing for no friction, in Figs. 3.10 a) and c). The corresponding coherence functions are shown in Figs. 3.10 b) and d).

The transient analysis was also carried out on the "3-D" finite element model with the bilinear model of the friction force enabling variable contact between the boring bar and the clamping house. To estimate the slip threshold, the average element length was calculated as $\bar{l}_e = 6.973 \cdot 10^{-3}$ [m], yielding the slip threshold $\delta = 1.743 \cdot 10^{-5}$ [m]. The bilinear model of the friction force was tested for four different values of the slip threshold: $1.743 \cdot 10^{-5}$ [m], $5 \cdot 10^{-5}$ [m], 10^{-5} [m] and $5 \cdot 10^{-6}$ [m]. The accelerance functions between the actuator voltage and the accelerations at the points of the active boring bar error sensor positions were estimated based on the transient analysis of the "3-D" finite element model (with the bilinear friction model and enabling variable contact between the boring bar and the clamping house) for the four different slip thresholds. Magnitude functions for these accelerance functions are plotted together with corresponding accelerance function for the finite element model, enabling variable contact between the boring bar and the clamping house while allowing for no friction in Figs. 3.11 a) and c). The corresponding coherence functions are shown in Figs. 3.11 b) and d).

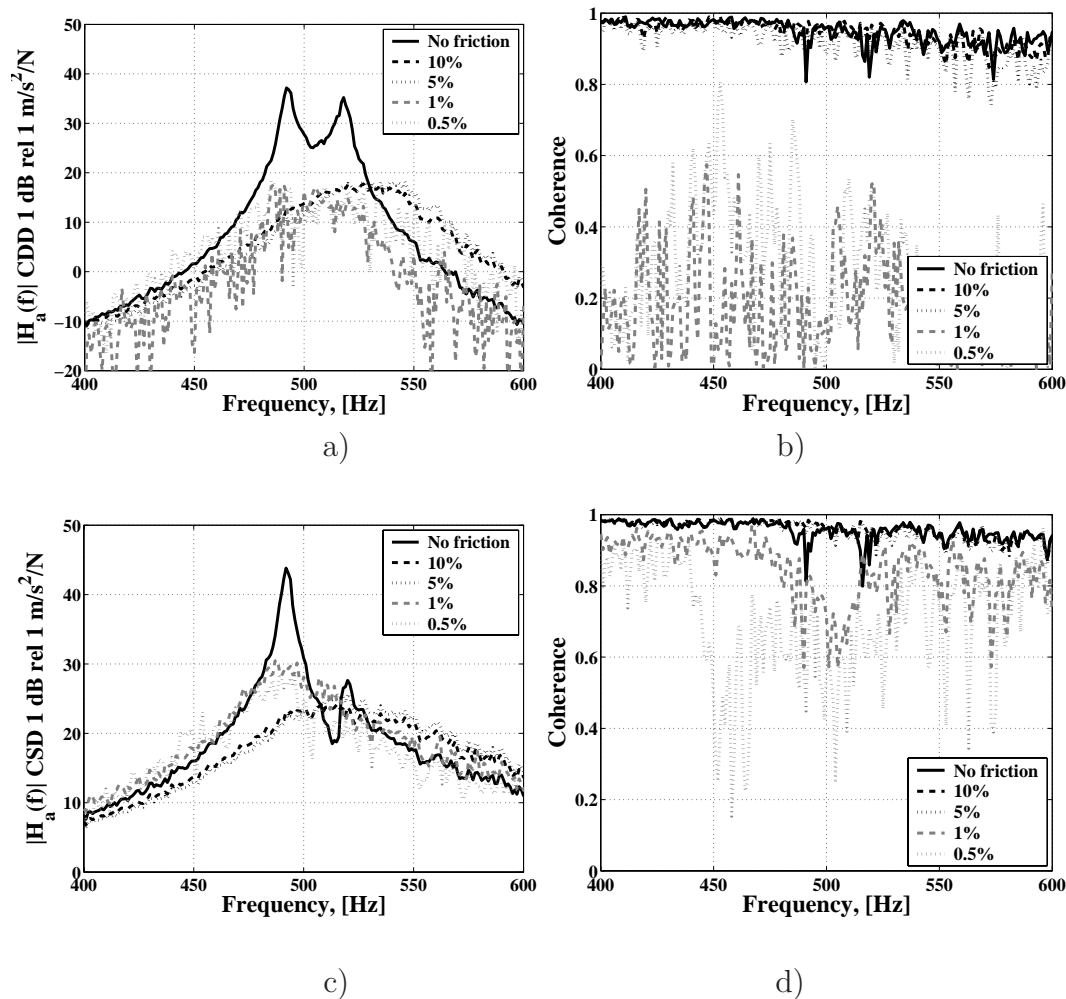


Figure 3.10: Magnitude of acceleration function estimates between the actuator voltage and acceleration in the error sensor positions a) in the cutting depth direction (CDD) and c) in the cutting speed direction (CSD). Coherence function estimates between the actuator voltage and the acceleration in the error sensor positions b) in the cutting depth direction (CDD) and d) in the cutting speed direction (CSD). Based on the transient analysis of the "3-D" finite element model of the active boring bar enabling variable contact between the boring bar and the clamping house and with the arctangent model of the friction force.

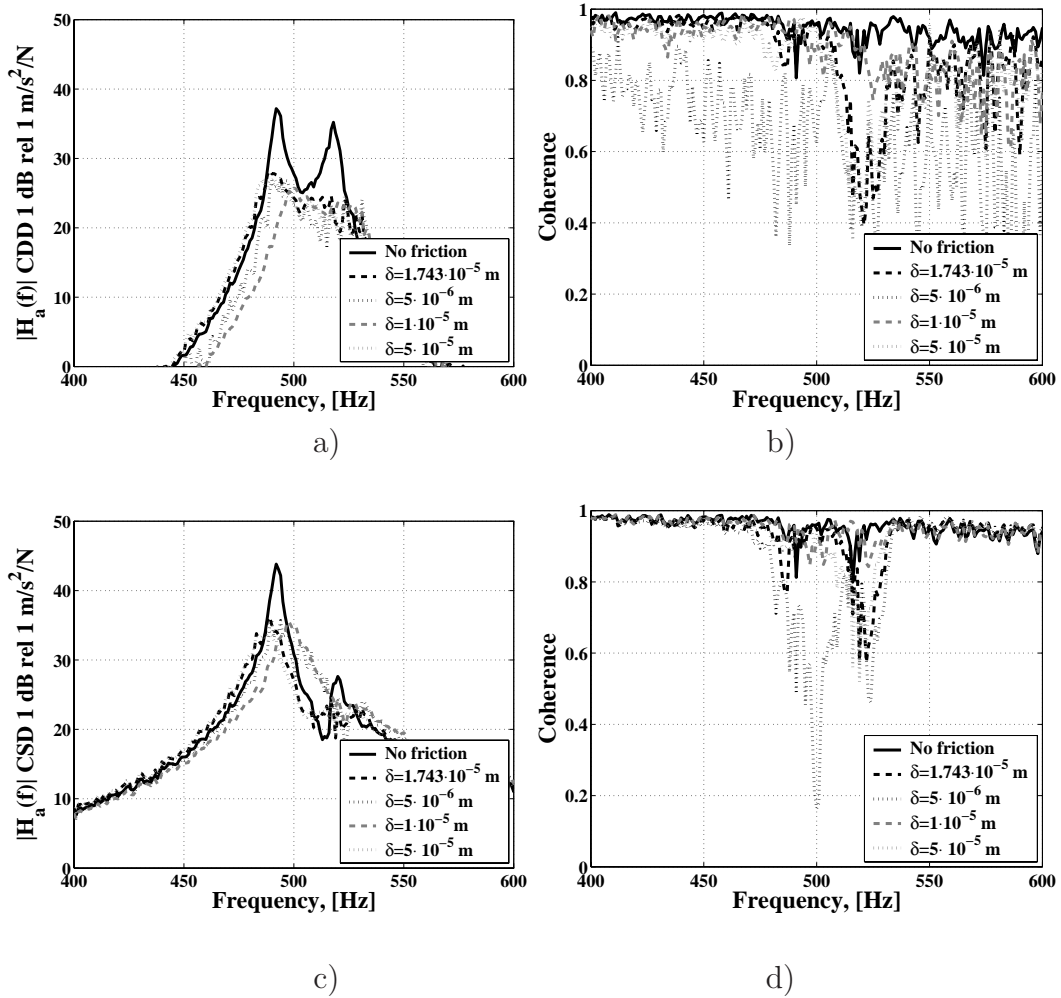


Figure 3.11: Magnitude of accelerance function estimates between the actuator voltage and the acceleration in the error sensor positions a) in the cutting depth direction (CDD) and c) in the cutting speed direction (CSD). Coherence function estimates between the actuator voltage and the acceleration in the error sensor positions b) in the cutting depth direction (CDD) and d) in the cutting speed direction (CSD). Based on the transient analysis of the "3-D" finite element model of the active boring bar enabling variable contact between the boring bar and the clamping house and with the bilinear model of the friction force.

3.4 Actuator Receptance

The "boring bar - actuator" interface receptance functions were estimated based on the transient response of the boring bar under applied random excitation voltage using the "3-D" finite element model of the boring bar enabling variable contact between the boring bar and the clamping house. The estimates of the receptance functions are produced using the calculated displacements and contact forces in the feed direction collected for the nodes of the boring bar finite element model corresponding to the actuator-boring bar engagement (see Fig. 3.12). The random error for the receptance functions estimated based on the "3-D" finite element model is shown in Fig. 3.13. The random error for the receptance function between the actuator voltage and the error receptance in the feed direction at the second "boring bar-actuator" interface at the resonance frequencies is 0.138 and 0.089 respectively. The random error of the receptance function between the actuator voltage and the error receptance at the first "boring bar-actuator" interface at the resonance frequencies is 0.047 and 0.081 respectively.

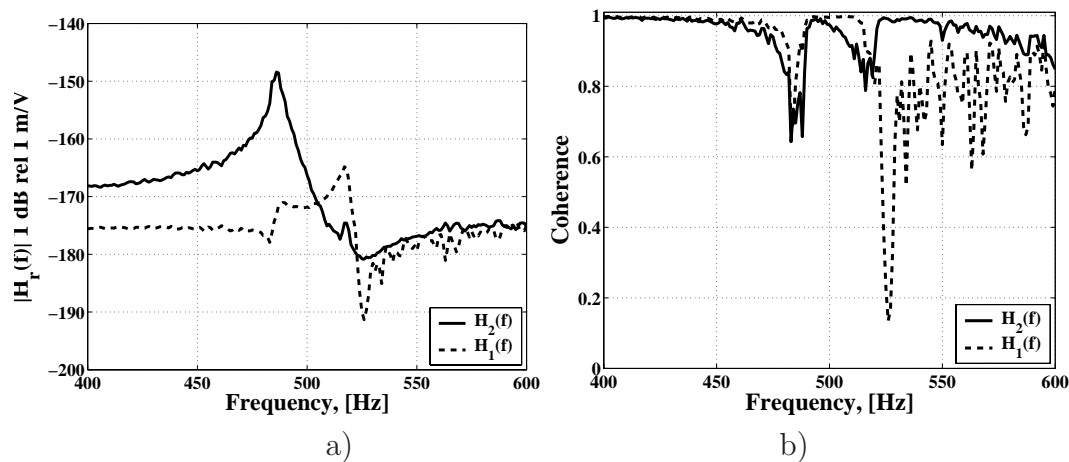


Figure 3.12: a) Magnitude function of receptance function estimates for the "boring bar - actuator" interfaces based on the "3-D" finite element model of the active boring bar enabling variable contact between the boring bar and the clamping house and b) corresponding coherence functions.

It is difficult if not impossible to measure the acceleration and the actuator force (in the feed direction) of the active boring bar in the interface between the actuator and the boring bar. For these reasons, the "boring bar - actuator" interfaces acceleration functions have not been estimated for the actual boring bar. The strain at positions close to the actuator interfaces of the actual active

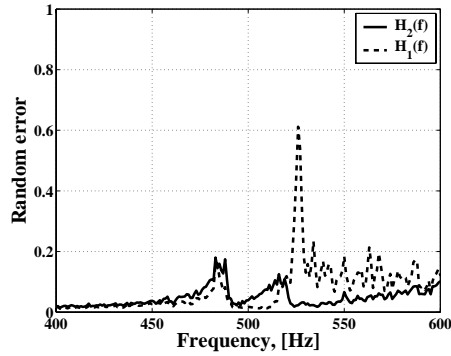


Figure 3.13: Random error for the receptances estimated based on the "3-D" finite element model of the the active boring bar enabling variable contact between the boring bar and the clamping house.

boring bar may, however, be measured. Thus, frequency response function estimates between the actuator voltage and the strain at four different positions (see Fig. 2.7) of the active boring bar have been produced based on both the linear "3-D" FE model and the model that enables variable contact between the clamping house and the boring bar. The magnitude functions for these frequency response functions are shown in Fig. 3.14. Also, frequency response function estimates between the actuator voltage and the strain at four different positions (see Fig. 2.7) have been estimated for the actual active boring bar, and they are illustrated in Fig. 3.15. Furthermore, in Fig. 3.16 the magnitude of the frequency response function estimates between the actuator voltage and the boring bar strain for both the "3-D" FE models and the actual boring bar are plotted together.

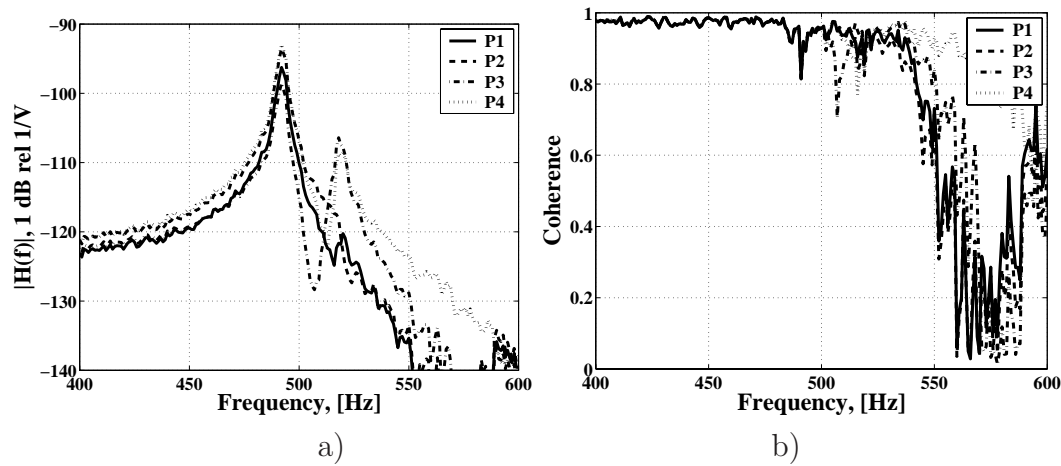


Figure 3.14: Magnitude of the frequency response function estimates between the actuator voltage and the boring bar strain, calculated based on the "3-D" FE model enabling variable contact between the boring bar and the clamping house, and b) the corresponding coherence function estimates.

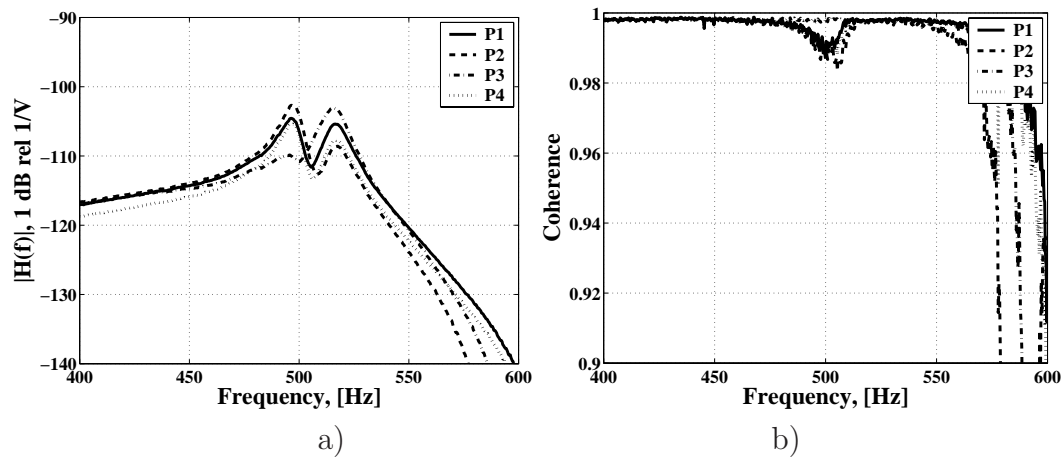


Figure 3.15: Magnitude of the frequency response estimates between the actuator voltage and the strain measured on the actual active boring bar, and b) the corresponding coherence function estimates.

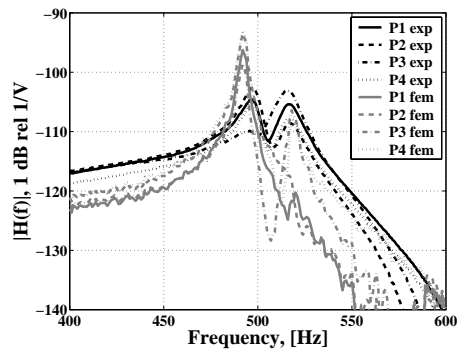


Figure 3.16: Magnitude of the frequency response estimates between the actuator voltage and the strain measured on the actual active boring bar and calculated based on the "3-D" FE model enabling variable contact between the boring bar and the clamping house.

Chapter 4

Summary and Conclusions

The "3-D" finite element model of the system "boring bar - actuator - clamping house" resulted in fairly accurate estimates of the boring bar's fundamental bending mode eigenfrequencies, 496.2 Hz and 529 Hz (see Table 3.1). Also, it provided estimates of the fundamental mode shapes that are well-correlated with the corresponding mode shapes extracted in the experimental modal analysis of the active boring bar (see Fig. 3.1 and the cross-MAC matrix in Eq. 3.1). The discrepancies between the natural frequency and mode shape estimates from the "3-D" finite element model and the experimental modal analysis may, for instance, be explained by differences between the actual active boring bar and the finite element model in dimensions and materials properties. Also, the fact that the attachment of the clamping house to the turret is modeled as infinitely rigid in the finite element model will introduce differences in the dynamic properties of the finite element model and the active boring bar.

Of significance is the ability to produce "3-D" finite element models of active boring bars which predict the control paths accurately. The following control paths have been considered: between the actuator input voltage and the output signal from the accelerometer measuring the boring bar vibration in the cutting speed direction close to the insert, and between the actuator input voltage and the output signal from the accelerometer measuring the boring bar vibration in the cutting depth direction close to the insert.

The ability to produce FE models of active boring bars enabling accurate modeling of the control paths is important for the development of efficient and accurate design procedure for active boring bars. The control path frequency response functions for the actual active boring bar were estimated (see Fig. 3.2 a)). The harmonic analysis of the linear "3-D" finite element model of the active boring bar results in control path accelerance estimates with magnitude levels significantly higher as compared to the control path accelerance estimates

of the actual active boring bar. This can be observed by comparing the control path acceleration estimates in Fig. 3.3 a) and Fig. 3.2 a). It is possible to reduce the magnitude of fundamental resonance frequency peaks in the control path acceleration function estimates produced based on the linear "3-D" finite element model by incorporating proportional damping (see Fig. 3.3 b)). However, compared to the control path frequency response functions for the actual active boring bar, the overall magnitudes of the proportionally damped finite element model control path acceleration functions are significantly higher (see Fig. 3.2 a) and Fig. 3.3 b)). Thus, the dynamic stiffness of the "3-D" finite element model with proportional damping is not sufficient.

The harmonic response simulation of the finite element model is carried out in MSC.MARC is only enabled for linear systems and uses only the boundary conditions as defined in the initial phase of the calculations. On the other hand, the transient response analysis allows for simulation of the active boring bar's response based on the "3-D" finite element model with variable contact between the clamping house and the boring bar. Time variable boring bar boundary conditions imposed by the clamping house in the finite element model are enabled. Compared to the linear FE models, the control path acceleration function estimates for the "3-D" finite element model of the active boring bar enabling variable contact between the clamping house and the boring bar display significantly improved correlation with the control path acceleration estimates of the actual active boring bar. This might be observed by comparing Figs. 3.2 a), 3.3 a), b) and 3.4 a) or from the Figure 3.6. It may also be observed that the "3-D" finite element model of the active boring bar allowing variable contact between the clamping house provides an approximation that is stiffer than the actual boring bar. This may be explained by the fact that boundary conditions used for the attachment of the clamping house are modeled as infinitely rigid in the FE model. However, in the lathe the attachment of the clamping house to the turret as well as the attachment of the turret to the slide, etc., cannot be considered completely rigid and, thus, flexibility is introduced. By comparing Fig. 3.2 a) and Fig. 3.4 a), it might be observed that the relative level between each of the resonance peaks for the two control path accelerances differ between the actual active boring bar and the FE model enabling variable contact. Thus, the orientation of the bending "modes" in the cutting depth/cutting speed plane may also differ between the actual active boring bar and the FE model enabling variable contact.

The possibility to further improve the accuracy of the "3-D" finite element model enabling variable contact between the clamping house and the boring bar by incorporating damping into it has also been addressed. The Coulomb friction force between the surfaces of the clamping house and the boring bar was introduced. To facilitate interpretation of the transient response analysis

results for the "3-D" finite element model with the Coulomb friction force, simulations of a simple nonlinear SDOF system were initially carried out for two different Coulomb friction force models; the arctangent model and the bilinear model. For a SDOF system with the Coulomb friction force approximated with the arctangent model, it can be observed from damping ratios estimated from simulations' results (see Table 3.2) that with an increasing excitation force level, from 100 N till 10000 N, the influence of the nonlinear friction force on the system's damping decreases. This is due to the fact that high excitation force levels induce vibration with the high velocities and the slip friction force magnitude is then negligible compared to the forces of the linear part of the system. At the constant excitation force level, different values of the relative sliding velocity ($\vartheta = 0.005\dot{w}_{max}$, $0.01\dot{w}_{max}$, $0.05\dot{w}_{max}$ and $0.1\dot{w}_{max}$) will introduce different levels of damping in the SDOF system (see Table 3.2 and Fig. 3.8 a). With a decreasing value of the relative sliding velocity, greater damping observed in the frequency response function estimates for the SDOF system (see Fig. 3.8 a)). Thus, the closer the arctangent friction model approximates the Coulomb friction force, the influence of the nonlinear friction force on the response of the system also increases which also is indicated by the coherence function estimates for the SDOF system in Fig. 3.8 b).

For a SDOF system with the Coulomb friction force approximated with the bilinear model, it can be observed from the natural frequencies estimated from simulations' results (see Table 3.3) that the influence of the nonlinear friction force on the systems stiffness will decrease with an increasing excitation force level. Thus, with an increasing force level the vibration displacement will increase and, as a consequence, the slip friction force magnitude will become more and more negligible compared to the forces of the linear part of the system. At the constant excitation force level, different values of the slip threshold δ from 10^{-4} m to 10^{-6} m will result in an increasing resonance frequency of the structure of approximately 9.5 %, i.e., from 501.5 Hz to 549 Hz (see Table 3.3 and Fig. 3.9 a)). With a decreasing value of the slip threshold, greater stiffness is observed in the frequency response function estimates for the SDOF system (see Fig. 3.9 a)). Thus, with a decreasing slip threshold the influence of the nonlinear friction force on the response of the system also increases which also is indicated by the coherence function estimates for the SDOF system in Fig. 3.9 b).

The dynamic behavior of the "3-D" finite element model of the system "boring bar - actuator - clamping house" including the Coulomb friction force and enabling variable contact is expected to be significantly more complicated to explain compared to the SDOF system. As time evolves, contact may occur or it may cease between nodes on the "3-D" surfaces of the clamping house and on the boring bar. Thus, the system has time-varying dynamic proper-

ties. Moreover, the "3-D" finite element model constantly changes its state, meaning that at a certain time instant contact is detected for some nodes, and friction force influence these nodes, while the other nodes, which were previously in contact, are separated and the friction ceases, etc. The introduction of the Coulomb friction force approximated with the arctangent model in the "3-D" finite element model of the active boring bar enabling variable contact between the clamping house and the boring bar resulted in significantly degraded control path acceleration function estimates for the set of used relative sliding velocities compared to the case with no friction force in the FE model (see Figs. 3.10 a) and 3.10 c)). However, replacing the arctangent model with the bilinear model in the "3-D" finite element model of the active boring bar enabling variable contact resulted in improved control path acceleration function estimates compared to the case with the arctangent friction model (c.f. Figs. 3.10 and 3.11). These control path acceleration function estimates display a lower correlation with acceleration function estimates for the actual active boring bar compared to the the "3-D" finite element model of the active boring bar enabling variable contact (compare Figs. 3.2 a), 3.10 a) 3.10 c), 3.11 a) and 3.11 c)). In the bilinear approximation, the friction force is proportional to the relative displacement between contacting bodies within the slip threshold δ . Vibrations result in relative displacements between the contacting nodes of the boring bar and clamping house. If the relative displacements are within the slip threshold δ , the friction force introduces an increase in the stiffness between contacting nodes as compared to no contact. The selection of slip threshold δ seems to influence the fundamental resonance frequencies of the system "boring bar - actuator - clamping house" (see Fig. 3.11 a) and Fig. 3.11 b)).

The "boring bar - actuator" interface receptance functions were estimated based on the transient response of the boring bar under applied random excitation voltage using the "3-D" finite element model of the boring bar enabling variable contact between the clamping house and the boring bar. The estimates of the receptance functions are produced using the calculated displacements and contact forces in the feed direction collected for the nodes of the actuator finite element model corresponding to the actuator-boring bar engagement (see Fig. 3.12). It is difficult if not impossible to measure the acceleration and force (in the feed direction) of the active boring bar in the interface between the actuator and boring bar. For this reason, the "boring bar - actuator" interfaces acceleration functions have not been estimated for the actual boring bar. The strain at positions close to the actuator interfaces of the actual active boring bar may, however, be measured. Thus, frequency response function estimates between the actuator voltage and the strain at four different positions (see Fig. 2.7) of the active boring bar may be produced based on both the "3-D" FE

model enabling variable contact between the clamping house and the boring bar (see Fig. 3.14 a)) and the actual active boring bar (see Fig. 3.15 a)). By comparing the frequency functions for the actual boring bar and the FE model, it follows that the FE model lacks damping and is slightly stiffer. Also, by examining Fig. 3.16 it follows that the orientation of the bending "modes" in the cutting depth/cutting speed plane is likely to differ between the actual active boring bar and the FE model enabling variable contact. One issue that seems to be of importance to address in future work, is to further improve the "3-D" FE model of the active boring bar by, e.g., the modeling of the boundary conditions imposed by the turret on the clamping house.

Acknowledgments

The present project is sponsored by Acticut International AB.

Bibliography

- [1] E. Marui, S. Ema, and S. Kato. Chatter vibration of lathe tools, part 1: General characteristics of chatter vibration. *Journal of Engineering for Industry*, 105:100–106, May 1983.
- [2] M. N. Hamdan and A. E. Bayoumi. An approach to study the effect of tool geometry on the primary chatter vibration in orthogonal cutting. *Journal of Sound and Vibration*, 128(3):451–469, 1989.
- [3] G. M. Zhang. Dynamic modeling and analysis of the boring machine system. *Journal of Engineering for Industry*, 1987.
- [4] S.A. Tobias. *Machine-Tool Vibration*. Blackie & Son, 1965.
- [5] H. E. Merritt. Theory of self-excited machine-tool chatter. *Journal of Engineering for Industry*, pages 447–454, 1965.
- [6] E. W. Parker. Dynamic stability of a cantilever boring bar with machine flats under regenerative cutting conditions. *Journal of Mechanical Engineering Science*, 1970.
- [7] P. N. Rao, U. R. K. Rao, and J. S. Rao. Towards improved design of boring bars, part 1: Dynamic cutting force model with continuous system analysis for the boring bar performance. *Journal of Machine Tool Manufacture*, 1988.
- [8] F. Kuster. Cutting dynamics and stability of boring bars. *Annals of the CIRP*, 39(1):361–366, 1990.
- [9] E. I. Rivin. Tooling structure: Interface between cutting edge and machine tool. *Annals of the CIRP*, 49(2):591–634, 2000.
- [10] C. M. Nicolescu. On-line identification and control of dynamic characteristics of slender workpieces in turning. *Journal of Material Processing Technology*, 58:374–378, 1996.

- [11] E. Al-Regib, J. Ni, and S.-H. Lee. Programming spindle speed variation for machine tool chatter suppression. *International Journal of Machine Tool & Manufacture*, 43(12):1229–1240, 2003.
 - [12] N. A. Ruud, R. Karlsen, K. Sørby, and C. Richt. Minimizing vibration tendencies in machining. *Technical Article at: <http://www.coromant.sandvik.com>*, 2005.
 - [13] *<http://www.teeness.no>*, 2005.
 - [14] S. G. Tewani, K. E. Rouch, and B. L. Walcott. A study of cutting process stability of a boring bar with active dynamic absorber. *International Journal of Machine Tools & Manufacture*, 35(1):91–108, 1995.
 - [15] D.R. Browning, I. Golioto, and N.B. Thompson. Active chatter control system for long-overhang boring bars. *Proceedings of SPIE*, 3044:270–280, 1997.
 - [16] I. Claesson and L. Håkansson. Adaptive active control of machine-tool vibration in a lathe. *IJAV-International Journal of Acoustics and Vibration*, 3(4):155–162, 1998.
 - [17] L. Pettersson, L. Håkansson, I. Claesson, and S.Olsson. Control of machine-tool vibration in a cnc lathe based on an active tool holder shank with embedded piezo ceramic actuators. *In Proceedings of the Eight International Congress on Sound and Vibration*, 2001.
 - [18] L. Pettersson, L. Håkansson, I. Claesson, and S.Olsson. Active control of boring bar vibration in cutting operations. *In Proceedings of the Ninth International Congress on Sound and Vibration, ICSV9*, 2002.
 - [19] H. Åkesson, T.Smirnova, I. Claesson, and L. Håkansson. On the development of a simple and robust active control system for boring bar vibration in industry. *IJAV-International Journal of Acoustics and Vibration*, 12(4):139–152, 2007.
 - [20] I. Claesson and L. Håkansson. Adaptive active control of machine-tool vibration in a lathe. *IJAV-International Journal of Acoustics and Vibration*, 3(4):155–162, 1998.
 - [21] B. W. Wong, B. L. Walcott, and K. I. Rouch. Active vibration control via electromagnetic dynamic absorbers. *IEEE*, page 868, 1995.
-

-
- [22] S. Nagano, T. Koizumi, N. Tsujiuchi T. Fujii, H. Ueda, and K. Steel. Development of a composite boring bar. *Composite Structures*, 38(1), 1997.
- [23] P.-O. H. Sturesson, L. Håkansson, and I. Claesson. Identification of the statistical properties of the cutting tool vibration in a continuous turning operation - correlation to structural properties. *Journal of Mechanical Systems and Signal Processing, Academic Press*, 11(3), July 1997.
- [24] J.R. Baker and K.E. Rouch. Use of finite element structural models in analyzing machine tool chatter. *Finite Elements in Analysis and Design*, (38):1029–1046.
- [25] R. Mahdavinejad. Finite element analysis of machine and workpiece instability in turning. *International journal of Machine Tools & Structure: Design, Research and Implementation*, (45):753–760.
- [26] http://www.efunda.com/Materials/piezo/material_data/matdata_output.cfm?Material_ID=PZT_5H.
- [27] *Low voltage co-fired multilayer stacks, rings and chips for actuation*. Piezomechnik, GmbH, 2006.
- [28] M.H. Hayes. *Statistical Digital Signal Processing and Modeling*. John Wiley Sons, Inc., 1996.
- [29] D.J. Ewins. *Modal Testing: Theory and Practice*. Research Studies Press, distributed by Wiley, 1984.
- [30] J.S. Bendat and A.G. Piersol. *Engineering Application of Correlation and Spectral Analysis*. John Wiley & Sons, second edition, 1993.
- [31] P.D. Welch. The use of fast fourier transform for the estimation of power spectra: A method based on time averaging over short modified periodograms. *IEEE Transaction on Audio and Electroacoustics*, pages 70–73, June 1967.
- [32] N.M.M. Maia and J.M.M. Silva. *Theoretical and Experimental Modal Analysis*. Research Studies Press Ltd., 1997.
- [33] L. Adrèn, L.Håkansson, A. Brandt, and I. Claesson. Identification of dynamic properties of boring bar vibrations in a continuous boring operation. *Journal of Mechanical Systems & Signal Processing*, 2004.
-

- [34] L. Adrèn, L.Håkansson, A. Brandt, and I. Claesson. Identification of motion of cutting tool in a continuous boring operation - correlation to structural properties. *Journal of Mechanical Systems & Signal Processing*, 18(4):903–927, 2004.
 - [35] J.F. Doyle. *Wave Propagation in Structures - Spectral Analysis Using Fast Discret Fourier Transforms*. Springer, second edition, 1997.
 - [36] D.J. Inman. *Engineering Vibration*. Prentice-Hall, second edition, 2001.
 - [37] C.R. Fuller, S.J. Elliott, and P.A. Nelson. *Active Control of Vibration*. Academic Press, Inc, 1996.
 - [38] C.H. Hansen and S.C. Snyder. *Active Control of Noise and Vibration*. E&FN SPON, 1997.
 - [39] R.W. Clough and J. Penzien. *Dynamics of Structures*. McGraw-Hill, second edition, 1993.
 - [40] <http://www.physikinstrumente.com/en/index.php>, 2007.
 - [41] *MSC.MARC Volume A: Theory and User's Information*. MSC.Software, 2005.
 - [42] R. L. Taylor O. S. Zienkiewicz and J.Z. Zhu. *The Finite Element Method: Its Basis and Fundamentals*. Butterworth-Heinemann, 2005.
 - [43] I. Doghri, A. Muller, and R.L. Taylor. A general three-dimensional contact procedure for implicit finite element codes. *Engineering Computations*, 15(2):233–259, 1998.
 - [44] K.Y. Wang, Y.L. Kang Q.H. Qin, J.S. Wang, and C.Y. Qu. A direct constraint-trefftz fem for analysing elastic contact problems. *International Journal for Numerical Methods in Engineering*, 63:1694–1718, April 2005.
 - [45] J. Williams. *Engineering Tribology*. Cambridge University Press, 2005.
 - [46] J. Chung and G. M. Hulbert. A family of single-step houbolt time integration algorithms for structural dynamics. *Comp. Meth. in App. Mech. Engg.*, 118, 1994.
 - [47] *Using MATLAB*. The MathWorks, Inc., 2002.
-